Reduced-order model of geometrically nonlinear flexible structures for fluid–structure interaction applications

Théo Flament, Jean-François Deü, Antoine Placzek, Mikel Balmaseda, Duc-Minh Tran

Reduced-order model of geometrically nonlinear flexible structures for fluid-structure interaction applications

T. Flament[a,b], J-F. Deü[b], A. Placzek[a], M. Balmaseda[c], D-M. Tran[a]

[a] *ONERA, Université Paris Saclay, Châtillon, F-92322, FRANCE*
[b] *LMSSC, Cnam, HESAM Université, Paris, F-75003, FRANCE*
[c] *ONERA, Université Paris Saclay, Meudon, F-92190, FRANCE*

Abstract

This paper deals with the numerical computation, via a reduced order models (ROM), of the vibrations of geometrically nonlinear structures triggered by the aeroelastic coupling with a fluid flow. The formulation of the ROM proposed in this paper is based on the projection on a basis of reduced dimension enhanced with dual modes. An explicit expression of the projected nonlinear forces is computed in a non-intrusive way based on the Implicit Condensation method. The resulting ROM is an improvement of the classical ICE method since the effects of membrane stretching are taken into account in the resolution of the dynamic equation of motion. Such a ROM aims to be adapted to follower aerodynamic unsteady loads. The construction of the ROM is first detailed and validated under several load cases on a Euler-Bernoulli beam with von Kármán hypothesis. Then a fluid-structure partitioned coupling on a two-dimensional example involving vortex-induced vibrations is considered to demonstrate the capability of such ROM to replace a nonlinear FE solver. In this paper, the limitations of the ICE method are highlighted in the examples treated, while the ROM proposed overcomes such limitations and captures accurately the dynamics.

Keywords: Computational dynamics, geometric nonlinearity, nonlinear model order reduction, fluid-structure interaction, aeroelasticity, dual

Email addresses: theo.flament@onera.fr (T. Flament), jean-francois.deu@cnam.fr (J-F. Deü), antoine.placzek@onera.fr (A. Placzek), mikel.balmaseda@onera.fr (M. Balmaseda), ducminht@gmail.com (D-M. Tran)

modes, Euler-Bernoulli/von Kármán beam

Acronyms:

CFD	Computational Fluid Dynamics
CSM	Computational Structural Dynamics
FE	Finite Element
FOM	Full Order Model
IC	Implicit Condensation
ICE	Implicit Condensation and Expansion
ICDual	Reduced-order model using dual modes along with the Implicit Condensation
ROM	Reduced Order Model
SVD	Singular Value Decomposition

1. Introduction

The research of better performances for future aircraft engines leads to larger fans and blades, therefore more flexible structures. The flexibility of such structures results in higher amplitudes of deformation. Therefore, the geometric nonlinearity of the structure cannot be neglected anymore and significantly alters the level of vibrations, having an impact on aeroelastic phenomena such as flutter and forced response. One way to perform an aeroelastic computation is to couple together two solvers, one for the fluid and one for the structure. Nevertheless, when dealing with industrial applications, the computational resources in time and memory of such coupling are too significant to be acceptable. Besides, most fluid solvers and structural solvers are not designed for the purpose of communicating with one another and the transfer of information from one solver to the other is often laborious. To overcome those limitations, an efficient approach is to couple the nonlinear fluid solver with a nonlinear reduced-order model (ROM) instead of a FE structural solver. To be efficient, the ROM has to be designed in a non-intrusive way so that it is independent of the FE model during the computation. The fluid dynamics can also be represented by lower fidelity models (e.g. Theodorsen or Lifting-line) or high-fidelity based reduced order models (e.g. data-driven, hybrid formulations). In this work, the fluid dynamics is not reduced and computed with an high-fidelity CFD solver. The paper focuses on the development of a nonlinear structural ROM. The literature suggests several methods to build reduced-order models tackling

structural geometric nonlinearities. One idea is to enhance the classical projection on a reduction basis containing the first linear normal modes of the structure by including additional modes aimed at capturing the nonlinearity, such as modal derivatives [1, 2, 3, 4] or dual modes [5, 6, 7, 8, 9]. Although it is a non-intrusive and flexible method, the difficulty lies in the selection of the additional modes. Another approach relies on invariant manifolds [10, 11, 12, 13] or spectral submanifolds [14, 15], both treating periodic vibrations at the resonance of linear normal modes. Such a method enables to precisely reach high-order amplitudes of displacements and treat internal resonances specifically. Nevertheless, aerodynamic forces are follower forces leading to a dependency of the load to the position. Considering a reduction method based on invariant manifolds, the load has to be either explicitly known leading to time dependent invariant manifolds, or is not considered in the construction of the model but is applied afterwards. Examples of such methods for fluid-structure interaction problems are found in [16, 17, 18]. Besides, such a method suggests to consider polynomial orders higher than 3, but for such orders the construction of the model is intrusive and requires specific accesses and operations inside the FE solver. Industrial CSM solvers do not provide such access. The intrusiveness is a limitation also encountered in hyper-reduction methods such as the Discrete Empirical Interpolation Method (DEIM) [19] which evaluates the nonlinearity only at a wisely selected degrees of freedom. The literature also refers to methods, such as the Proper Orthogonal Decomposition (POD) method [20, 21, 22, 23], based on the results from high-fidelity simulations. The major drawback is that a preliminary database of representative solutions is required to determine the projection basis, the former being computationally expensive and directly dependent on the set of parameters of the test case.

The ROM used in this paper is built by projection on a reduction basis containing both the linear normal modes of the structure and additional dual modes identified from nonlinear static computations with external loads defined by combinations of linear modes shapes. In the frame of finite deformations with large displacements and small strains, the nonlinear internal geometric forces are approximated by a third-order polynomial of generalized coordinates. The coefficients of the polynomial may be identified with the *Implicit Condensation* (IC) method [24]. The basic IC method described in the article [24] is restricted to only the first bending modes of the structure. An *Expansion* step (ICE)[25], comparable to a static compensation, is usually performed to rebuild the missing in-plane displacements a posteriori.

It is a non-intrusive method that is classically performed to build reduced-order models for large structures and was for instance applied to compute the aeroelastic response of a wing in [26]. However, the in-plane dynamics is simply rebuilt a posteriori with this approach and not included into the reduced equation of the dynamics during the resolution. For this reason, such a method has limited efficiency to capture the dynamics of the membrane stretching. An *Inertial Compensation* [27] has been suggested in the literature to consider the in-plane dynamics into the equations of the bending modes, changing the nature of the reduced equations. A *Force Compensation* [28] was also recently proposed to take into account follower forces with known shape.

In the present paper, a pertinent set of dual modes is added in the reduction basis. The aim is to compute the in-plane vibrations directly in the reduced equations of the dynamics. Such modes contain information on the nonlinear coupling between the bending and the membrane displacements. Doing so, the approximated post-processing *Expansion* step is no longer useful. The reduced-equations compute a richer dynamics and can be integrated with classical time integration schemes. Besides, the reduction basis is determined in a non-intrusive way and follower forces do not need special treatment apart from their projection into the reduction basis. The coefficients of the projected nonlinear forces are determined with a force-based method. Such a strategy has been used before but with condensed models containing only the transverse linear modes [24] and not both transverse and in-plane displacements like here. First, the ability of such a ROM to characterize the nonlinear vibrations of an Euler-Bernoulli/von Kármán cantilever beam is studied under different external forcing cases. Beam models are indeed computationally cheap and enable to understand the phenomena at stake such as the bending/membrane coupling and its impact on the performances of the ROMs [29, 30]. Subsequently, the ROM is coupled with a nonlinear fluid solver to compute the dynamical vibrations of the nonlinear beam, subjected to the unsteady forcing of a von Kármán vortex street in the wake of a fixed cylinder.

2. Classical projection-based reduced-order models

The behavior of the structure is studied thanks to a classical finite element model, whose degrees of freedom in displacement, written $\mathbf{u}$, verify the equation of the dynamics :

$$\mathbf{M}\ddot{\mathbf{u}} + \mathbf{C}\dot{\mathbf{u}} + \mathbf{K}\mathbf{u} + \mathbf{f}_{\text{nl}}(\mathbf{u}) = \mathbf{f}_{\text{a}}(\mathbf{u}, \dot{\mathbf{u}}), \tag{1}$$

where $\mathbf{M}$,$\mathbf{C}$, $\mathbf{K}$, $\mathbf{f}_{\text{nl}}$ and $\mathbf{f}_{\text{a}}$ are respectively the mass matrix, the damping matrix, the elastic stiffness matrix, the internal nonlinear forces vector and the aerodynamic forces vector in the case of an aeroelastic problem.

One method to build a reduced order model is to project the equations of the dynamics on a well-chosen basis of reduced dimension $\mathbf{V}$. The displacements degrees of freedom are approximated by $\mathbf{u} \approx \mathbf{V}\mathbf{q}$ where $\mathbf{q}$ are called the generalized coordinates. The internal forces can be decomposed as the sum of a linear component $\mathbf{K}\mathbf{u}$ and a geometric nonlinear component $\mathbf{f}_{\text{nl}}(\mathbf{u})$. After such decomposition and projection, the equation of the dynamics becomes :

$$\underbrace{\mathbf{V}^T\mathbf{M}\mathbf{V}}_{\widetilde{\mathbf{M}}}\ddot{\mathbf{q}} + \underbrace{\mathbf{V}^T\mathbf{C}\mathbf{V}}_{\widetilde{\mathbf{C}}}\dot{\mathbf{q}} + \underbrace{\mathbf{V}^T\mathbf{K}\mathbf{V}}_{\widetilde{\mathbf{K}}}\mathbf{q} + \underbrace{\mathbf{V}^T\mathbf{f}_{\text{nl}}(\mathbf{V}\mathbf{q})}_{\widetilde{\mathbf{f}}_{\text{nl}}(\mathbf{q})} = \underbrace{\mathbf{V}^T\mathbf{f}_{\text{a}}}_{\widetilde{\mathbf{f}}_{\text{a}}}. \tag{2}$$

The reduction matrix $\mathbf{V}$ contains only few vectors, therefore the projected matrices $\widetilde{\mathbf{M}}$, $\widetilde{\mathbf{C}}$ and $\widetilde{\mathbf{K}}$ have negligible dimensions compared to the initial problem. The aerodynamic forces $\mathbf{f}_{\text{a}}$ are obtained during the aeroelastic coupling from the fluid solver used in the partitioned approach. In section 5, local arbitrary loads are first considered for the structural tests. Representative aerodynamic forces are then considered in section 6.

2.1. Determination of the reduction basis

Mechanical vibrations can be characterized by linear normal modes $\mathbf{\Phi} = \{\boldsymbol{\phi}_1, \cdots, \boldsymbol{\phi}_n\}$, solutions of the eigenvalue equation :

$$\left(\mathbf{K} - \omega_i^2\mathbf{M}\right)\boldsymbol{\phi}_i = \mathbf{0}. \tag{3}$$

where ω_i are the eigen-angular frequencies.

When the amplitudes of displacement are small and the geometric nonlinearity can be neglected, the problem is linear. In such a case, a satisfactory choice to represent the dynamical behavior is a reduction basis containing only the first linear normal modes, whose frequencies belong to the excitation band. On the contrary, when the geometric nonlinearity is significant, a

coupling may appear between some low- and high-frequency modes. Consequently, the first linear modes are no longer sufficient to capture the whole dynamics and the reduction basis has to be enriched by other modes in order to account for the coupling between the modes.

The data added to the reduction basis should contain information on the coupling between several linear normal modes and should not depend on specific loading cases. One idea is to capture the nonlinearity in the vicinity of the linear normal modes, using modal derivatives. Modal derivatives are second-order Taylor expansions around the equilibrium position of the structure and can be computed in several ways, taking or not the inertia into account [1, 2, 3, 31]. A drawback of modal derivatives is their plurality. The number of modal derivatives drastically increases with the number of linear normal modes considered. In a basis containing n linear normal modes, $n(n+1)/2$ modal derivatives exist. Although a criterion to reduce their number is proposed in [4], the size of the resulting reduction basis may not be as small as expected for an efficient ROM. Another possibility to enrich the reduction basis is the use of dual modes [5, 6, 7, 8, 9, 32, 33]. The latter are computed from nonlinear static solutions obtained by imposing external loads to the structure, whose distribution involves the first linear normal modes so that the loads are not case-dependent. Those nonlinear static solutions contain information on the geometric nonlinearity that is missing from the linear normal modes. Such information is extracted and a SVD is performed. Eventually, the SVD modes with the highest singular values as well as the modes associated with a significant linearized strain energy are the dual modes selected to enrich the reduction basis. An interesting comparison of basis sizes between the modal derivatives and the dual modes for beam and shell examples is found in [34].

2.2. Approximation of the projected nonlinear forces

When a partitioned fluid-structure coupling is considered, the fluid solver interacts with an external FE solver to compute the displacement of the structure at every sub-iteration of coupling. The transfer of data between the fluid and the structure solvers is not an easy task and a significant advantage is to use a *non-intrusive* ROM, independent from any FE solver during the online stage. However, since the evaluation of the projected nonlinear forces $\mathbf{V}^T\mathbf{f}_{\text{nl}}(\mathbf{Vq})$ requires back-and-forth exchanges between the ROM and the FEM variables, the ROM resulting from Eq.(2) is therefore intrusive. More

precisely, the physical displacements $\mathbf{u} \approx \mathbf{V}\mathbf{q}$ have first to be assembled before the evaluation of the nonlinear forces $\mathbf{f}_{\text{nl}}(\mathbf{V}\mathbf{q})$ by the FE solver, which are finally projected again in the reduced space. It would be of great interest to know the explicit expression of the projected nonlinear forces $\widetilde{\mathbf{f}}_{\text{nl}}(\mathbf{q})$ as a function of the generalized coordinates. Thus the structural problem could be solved directly in the reduced space:

$$\widetilde{\mathbf{M}}\ddot{\mathbf{q}} + \widetilde{\mathbf{C}}\dot{\mathbf{q}} + \widetilde{\mathbf{K}}\mathbf{q} + \widetilde{\mathbf{f}}_{\text{nl}}(\mathbf{q}) = \widetilde{\mathbf{f}}_{\text{a}}. \tag{4}$$

Considering geometric nonlinearities in the frame of finite displacements (small strains, large displacements and large rotations) and the Saint Venant-Kirchhoff model, the nonlinear forces resulting from geometric nonlinearities is a third-order polynomial function of the generalized coordinates [35, 36]. Writing $\widetilde{f}^k_{\text{nl}}(\mathbf{q})$ the k^{th} coordinate of the projected nonlinear force, its expression can be written explicitly from the generalized coordinates:

$$\widetilde{f}^k_{\text{nl}}(\mathbf{q}) = \sum_{i=1}^{n} \sum_{j=i}^{n} \beta^k_{ij} q_i q_j + \sum_{i=1}^{n} \sum_{j=i}^{n} \sum_{m=j}^{n} \gamma^{\ k}_{ijm} q_i q_j q_m, \tag{5}$$

with n the number of modes in the reduction basis, while β^k_{ij} and γ^k_{ijm} are respectively the quadratic and cubic coefficients of the polynomial approximation of the nonlinear forces. Appendix B provides a formulation of the Jacobian of the projected nonlinear forces that will be exploited for the resolution of the nonlinear systems. Nevertheless, the coefficients β^k_{ij} and $\gamma^{\ k}_{ijm}$ have yet to be determined. Two methods are found in the literature. The first one involves the determination of the coefficients with imposed displacements, called STEP [35] and including in some cases precautions for use with 3D cases [37, 29, 38]. In this method, the coefficients of the polynomial are determined specifically by imposing to the structure various displacements with the shape of well-chosen linear combinations of the linear normal modes [39, 40, 41]. The second method relies on prescribed loads to the structure to determine the coefficients. Such a method is called *Implicit Condensation* [24], and an *Expansion* [25] step has been proposed. Prescribed loads instead of displacements are imposed to the structure, with load distributions derived from the linear normal modes. Both the nonlinear static solutions and the nonlinear forces are computed. The generalized coordinates on the reduction basis are extracted from the nonlinear static solutions by means of a least-squares method. The coefficients β^k_{ij} and γ^k_{ijm} are finally obtained

by identification between the formula (5) and the nonlinear forces computed with the FE solver. A short description of the IC and ICE methods is proposed in the following subsections. Such methods are at the foundation of the ROM proposed in this paper and the performance of these different methods in terms of accuracy will be compared on selected test cases in section 5 and 6.

2.3. Implicit Condensation and Expansion (ICE) method

The idea of the *Implicit Condensation* method [24] is to select in the reduction basis the first n_b linear normal modes: $\mathbf{\Phi} = [\boldsymbol{\phi}_1, \cdots, \boldsymbol{\phi}_{n_\mathrm{b}}]$ corresponding usually to bending modes for slender structures. Then the nonlinear forces coefficients of Eq.(5) are identified thanks to static nonlinear displacements obtained under load cases. A set of n_L loading cases $\mathbf{f}_\mathrm{ext}^{(1)}$, $\mathbf{f}_\mathrm{ext}^{(2)}$, $\cdots$, $\mathbf{f}_\mathrm{ext}^{(n_\mathrm{L})}$ are introduced. The distribution of each load case $\ell \in [1, n_\mathrm{L}]$ is defined as a linear combination of the linear normal modes:

$$\mathbf{f}_\mathrm{ext}^{(\ell)} = \alpha_1^{(\ell)}\boldsymbol{\phi}_1 + \alpha_2^{(\ell)}\boldsymbol{\phi}_2 + \cdots + \alpha_{n_\mathrm{b}}^{(\ell)}\boldsymbol{\phi}_{n_\mathrm{b}}. \tag{6}$$

The determination of the quadratic and cubic coefficients of the reduced nonlinear forces is carried out by identification between Eq.(5) and the projection of the internal nonlinear forces obtained with the nonlinear static computations under the loads (6): $\mathbf{K}\mathbf{u}^{(\ell)} + \mathbf{f}_\mathrm{nl}(\mathbf{u}^{(\ell)}) = \mathbf{f}_\mathrm{ext}^{(\ell)}$. More details about the identification of the polynomial coefficients are given later in section 3.2.

In the original IC method, the reduction basis comprises exclusively bending modes. Therefore, the contribution of the other modes, for instance the membrane modes of beam or shells, is omitted in the result. The specificity of the ICE method is to improve the solution obtained with the IC method by adding a post-processing step whose aim is to enrich the displacement solution with information on the membrane displacement that is not contained in the few linear normal modes selected. The assumption is that the total displacement $\mathbf{u}$ is the sum of the approximated solution obtained with the first linear normal modes selected $\mathbf{u}_\mathrm{b}$ and a set of *Expansion* modes $\mathbf{\Psi}$ multiplied by generalized coordinates $\boldsymbol{\eta}$. Such generalized coordinates are defined as quadratic functions of the generalized coordinates associated to the selected modes $\mathbf{\Phi}$:

$$\mathbf{u} = \mathbf{u}_\mathrm{b} + \mathbf{u}_\mathrm{m} = \sum_{k=1}^{n_\mathrm{b}} \boldsymbol{\phi}_k q_k + \sum_{k=1}^{n_\mathrm{m}} \boldsymbol{\psi}_k \eta_k = \boldsymbol{\Phi}\mathbf{q} + \boldsymbol{\Psi}\boldsymbol{\eta}. \tag{7}$$

The total displacement can thus be interpreted as a quadratic mapping. The first linear bending modes $(\boldsymbol{\phi}_k)_{k\in[1,n_\mathrm{b}]}$ are known as well as the corresponding generalized coordinates q_k. On the contrary, the modal amplitudes of the *Expansion* modes $\boldsymbol{\Psi}$ are obtained as quadratic combinations of the modal amplitudes relative to the first linear normal modes q_k:

$$\boldsymbol{\eta} = \begin{bmatrix} q_1^2 & q_1 q_2 & \cdots & q_1 q_{n_\mathrm{b}} & q_2^2 & q_2 q_3 & \cdots & q_{n_\mathrm{b}}^2 \end{bmatrix}^T. \tag{8}$$

Nevertheless, the *Expansion* modes $(\boldsymbol{\psi}_q)_{q\in[1,n_\mathrm{m}]}$ are not known and have to be determined during the construction of the reduced-order model. To this end, a matrix $(\mathbf{Q}_\mathrm{m})_{(n_\mathrm{m}\times n_\mathrm{L})}$ (respectively $(\mathbf{Q}_\mathrm{b})_{(n_\mathrm{b}\times n_\mathrm{L})}$) is built, whose rows are the generalized amplitudes $(\eta_q)_{q\in[1,n_\mathrm{m}]}$ (respectively $(q_k)_{k\in[1,n_\mathrm{b}]}$) and the columns their values for each static solutions associated to a loading $\mathbf{f}_\mathrm{ext}^{(\ell)}$. Introducing the matrix $(\mathbf{U}_\mathrm{t})_{(n_\mathrm{b}\times n_\mathrm{L})}$ whose columns are the nonlinear static solutions $\mathbf{u}^{(\ell)} = \mathbf{u}_\mathrm{b}^{(\ell)} + \mathbf{u}_\mathrm{m}^{(\ell)}$ leads to the matrix system:

$$\mathbf{U}_\mathrm{t} = \boldsymbol{\Phi}\mathbf{Q}_\mathrm{b} + \boldsymbol{\Psi}\mathbf{Q}_\mathrm{m}. \tag{9}$$

The *Expansion* modes used for the ICE reconstruction of the displacement are then obtained by:

$$\boldsymbol{\Psi} = \left[\mathbf{U}_\mathrm{t} - \boldsymbol{\Phi}\mathbf{Q}_\mathrm{b}\right]\mathbf{Q}_\mathrm{m}^{+}, \tag{10}$$

where $\mathbf{Q}_\mathrm{m}^{+}$ is the pseudo-inverse of $\mathbf{Q}_\mathrm{m}$. In [25], the authors suggest to use the first bending modes in the reduction basis, therefore the *Expansion* modes are mostly modes with a predominant membrane contribution. During the temporal resolution of the dynamics equations of motion, the structural response in terms of modal bending amplitudes $\mathbf{u}_\mathrm{b}$ is determined. The corresponding membrane displacements η_k are then computed with Eq.(8) and finally the total displacement is rebuilt as $\mathbf{u} = \mathbf{u}_\mathrm{b} + \mathbf{u}_\mathrm{m}$. Equation (8) is a quadratic mapping or quadratic modal condensation [42]. Since the internal forces are cubic in the degrees of freedom and the displacement is a quadratic mapping of the generalized coordinates, truncating the polynomial development of the projected nonlinear forces at the third-order is an approximation and higher-orders are sometimes necessary [43]. Besides, for cantilever structures, the IC method with bending modes and its expansion ICE becomes inaccurate

in the dynamic case with large axial displacement, which will be highlighted in the examples of the present paper. Indeed, since only bending modes are included in the reduced basis, there is no equation relative to the membrane dynamics in the reduced system. In order to address this problem, the approach considered in this paper rely on the definition of a projection basis including the first linear modes and additional dual modes. The polynomial coefficients for the approximation of the nonlinear forces are then identified for this expanded basis and the membrane effects are taken into account during the resolution of the equation of motion instead of being post-processed like in the ICE method.

3. Implicit Condensation with dual modes (ICDual)

In this section, a reduction method using the dual modes determining the nonlinear coefficients with imposed loads is detailed. Such method will be referred to as ICDual in the rest of the paper. First, the determination of the dual modes to improve the reduction basis is detailed. Then, two methods to determine the coefficients of the projected nonlinear forces using prescribed loads are proposed. The first method is similar to the Implicit Condensation method exploited the FE nonlinear forces and the second is based on the tangent stiffness matrices. The methods proposed in this paper enable to reuse the nonlinear static solutions computed during the process of selection of the dual modes, to determine the coefficients of the projected nonlinear forces.

3.1. Enhancing the projection basis with dual modes

This section details the determination of dual modes which are added to the projection basis in order to capture the geometric nonlinearity without resorting to a post-processing step.

A set of external forces are first applied to the structure as a combination of the first linear normal modes $(\boldsymbol{\phi})_{i\in[1,n_\mathrm{b}]}$ of the structure:

$$\forall \ell \in [1, n_\mathrm{L}] \quad \mathbf{f}_\mathrm{ext}^{(\ell)} = \mathbf{K}\left(\sum_{i=1}^{n_\mathrm{b}} \alpha_i^{(\ell)} \boldsymbol{\phi}_i \right), \tag{11}$$

where $\alpha_i^{(\ell)}$ are weighting coefficients. The associated nonlinear static solutions $\mathbf{u}_\mathrm{s}^{(\ell)}$ are computed from the equation:

$$\mathbf{K}\mathbf{u}_\mathrm{s}^{(\ell)} + \mathbf{f}_\mathrm{nl}(\mathbf{u}_\mathrm{s}^{(\ell)}) = \mathbf{f}_\mathrm{ext}^{(\ell)}. \tag{12}$$

From those nonlinear static solutions, generalized coordinates $\mathbf{q}^{(\ell)}$ on the modes of the reduction basis are extracted by least-squares approximations since $\mathbf{u}_{\mathrm{s}}^{(\ell)} \approx \mathbf{\Phi q}^{(\ell)}$. The remainder of the approximation is written $\mathbf{r}^{(\ell)}$. For each nonlinear static solution, we have

$$\mathbf{u}_{\mathrm{s}}^{(\ell)} = \mathbf{\Phi q}^{(\ell)} + \mathbf{r}^{(\ell)}, \tag{13}$$

and all the remainders $\mathbf{r}^{(\ell)}$ are gathered in a matrix, from which a singular value decomposition (SVD) is computed:

$$\left[\mathbf{r}^{(1)}, \ \cdots, \ \mathbf{r}^{(n_{\mathrm{L}})}\right] = \left[\mathbf{d}_1, \ \cdots, \ \mathbf{d}_{n_{\mathrm{p}}}\right] \mathrm{diag}(\sigma_1, \sigma_2, \cdots, \sigma_{n_{\mathrm{p}}}) \mathbf{W}^T, \tag{14}$$

where $(\sigma_i)_{i\in[1,n_{\mathrm{p}}]}$ are the non-null singular values ordered from the largest to the smallest, $(\mathbf{d}_i)_{i\in[1,n_{\mathrm{p}}]}$ the left singular vectors of the decomposition and $\mathbf{W}^T$ containing the right singular vectors, of shape $(n_{\mathrm{p}} \times n_{\mathrm{L}})$. The projection of the remainder vectors $\mathbf{r}^{(\ell)}$ on the SVD basis vectors is the following:

$$\mathbf{r}^{(\ell)} = \sum_{k=1}^{n_{\mathrm{p}}} \beta_k^{\ell} \mathbf{d}_k, \tag{15}$$

with $\beta_k^{\ell} = \sigma_k W_{\ell k}$. Considering $\mathcal{E}_r$ the sum of the linearized strain energy of all the nonlinear remainder displacements $\mathbf{r}^{(\ell)}$ we can write:

$$\mathcal{E}_r = \sum_{\ell=1}^{n_{\mathrm{L}}} \mathbf{r}^{(\ell)^T} \mathbf{K} \mathbf{r}^{(\ell)} = \sum_{k=1}^{n_{\mathrm{p}}} \underbrace{\left(\sum_{\ell=1}^{n_{\mathrm{L}}} {\beta_k^{\ell}}^2 \mathbf{d}_k^T \mathbf{K} \mathbf{d}_k \right)}_{E_k}, \tag{16}$$

since $\forall (k,j) \in [1, n_{\mathrm{p}}]^2, \mathbf{d}_k^T \mathbf{d}_j = \delta_{kj}$.

As explained in [5], the dual modes selected for inclusion in the reduction basis are the vectors $\left(\mathbf{d}_i\right)_{i\in[1,n_{\mathrm{p}}]}$ with the largest singular values σ_i and those contributing the most to the linearized strain energy, i.e. those leading to the largest values of E_i. The vectors $\left(\mathbf{d}_i\right)_{i\in[1,n_{\mathrm{p}}]}$ ranked by decreasing singular values are selected until the desired precision is obtained. To do so, the reduction basis $\mathbf{\Phi}$ is supplemented by the vectors $\left(\mathbf{d}_1, \mathbf{d}_2, ..., \mathbf{d}_k\right)$ to form the matrix $\mathbf{V}^{(k)} = [\mathbf{\Phi}, \mathbf{d}_1, \cdots, \mathbf{d}_k]$. Then the matrix $\mathbf{U}_s$ collecting all static displacements $\mathbf{u}_{\mathrm{s}}^{(\ell)}$ is approximated as $\mathbf{V}^{(k)}\mathbf{Q}^{(k)}$ by a least squares method.

The dual modes are first selected with respect to the following criterion to ensure that the static solutions are properly approximated when adequate linear and dual modes are included in the basis:

$$\frac{\max(|\mathbf{U_s} - \mathbf{V}^{(k)}\mathbf{Q}^{(k)}|)}{\max(|\mathbf{U_s}|)} < \varepsilon_\sigma \tag{17}$$

The second step is to satisfy a sufficient contribution to the linearized strain energy. The remaining dual modes candidates are ordered by decreasing linearized strain energy contributions and are added to the reduction basis until the following error is below the threshold ε_E:

$$\frac{1}{\mathcal{E}_r}\left(\mathcal{E}_r - \sum_{i=1}^{k} E_i\right) < \varepsilon_E \tag{18}$$

with E_i the contribution to the total linearized strain energy defined in (16).

The new reduction basis is finally the concatenation $\mathbf{V} = [\mathbf{\Phi}, \mathbf{\Phi}_{\text{dual}}]$ of the first linear normal modes $\mathbf{\Phi}$ and the selection of dual modes $\mathbf{\Phi}_{\text{dual}}$ satisfying both criteria. The second and last step in the construction of the ROM is the determination of the explicit expression of the projected nonlinear forces using the *Implicit Condensation* method presented in section 2.3.

3.2. Computation of the nonlinear forces coefficients

The coefficients of the nonlinear forces approximation are computed similarly to the IC method in the sense that prescribed loads are applied to the structure. However, the reduction basis considered in the present work does not only contain linear normal modes, but also dual modes. Here, the loads are not imposed on the entire basis containing both linear normal modes and dual modes as suggested in [24, 8], but only on the linear normal modes. Indeed, applying loads to the dual modes produces internal forces whose amplitudes differ by several orders of magnitude from those associated to linear modes. The choice of the weighting coefficients becomes tricky and alters strongly the results.

In this paper, external loads are therefore prescribed only from a combination of linear modes, but displacements associated to dual modes are also included in the static solutions because of the nonlinear coupling. The same loads as those used for the determination of the dual modes Eq.(11) can thus be reused and possibly supplemented by additional load cases. With such distribution of loads based on the linear modes, the ROM can be used

for different load cases, such as aerodynamic forces for instance since the prescribed loads in Eq.(11) are rather generic. Besides, the product with the stiffness matrix in provides an estimation of the amplitude of the real physical displacement. Indeed, if the geometric nonlinearity was neglected, the displacement obtained by such a load case would exactly be the distribution imposed by the linear combination of modes $\sum_{i=1}^{n_\mathrm{b}} \alpha_i^{(\ell)} \boldsymbol{\phi}_i$. Since geometrical nonlinearities affect the static displacement and generally result in smaller displacements or with similar order of magnitude than linear ones, the previous remark gives an upper limit to the order of magnitude of the displacement. This observation provides a strategy to select the coefficients $\alpha_i^{(\ell)}$ so that the loads imposed are large enough to trigger geometric nonlinearities, and not too large to remain within the scope of acceptable yields stresses for the material. From this set of n_L external loadings, the n_L nonlinear static displacements are obtained by solving with a Newton-Raphson algorithm the nonlinear static equations:

$$\mathbf{K}\mathbf{u}_\mathrm{s}^{(\ell)} + \mathbf{f}_\mathrm{nl}(\mathbf{u}_\mathrm{s}^{(\ell)}) = \mathbf{f}_\mathrm{ext}^{(\ell)}, \tag{19}$$

Then the associated generalized coordinates $\mathbf{q}^{(\ell)}$ are computed by a least squares approximation using the pseudo-inverse of $\mathbf{V}$ from the equation:

$$\mathbf{q}^{(\ell)} = (\mathbf{V}^T\mathbf{V})^{-1}\mathbf{V}^T\mathbf{u}_\mathrm{s}^{(\ell)}. \tag{20}$$

At this point n_L couples $\left(\mathbf{q}^{(\ell)}, \mathbf{f}_\mathrm{nl}(\mathbf{u}_\mathrm{s}^{(\ell)})\right)$ are determined and satisfy the following system for the unknowns β_{ij}^k and γ_{ijm}^k:

$$\widetilde{f}_\mathrm{nl}^k(\mathbf{q}^{(\ell)}) = \mathbf{V}_k^T\mathbf{f}_\mathrm{nl}(\mathbf{V}\mathbf{q}^{(\ell)}) = \sum_{i=1}^{n}\sum_{j=i}^{n}\beta_{ij}^k q_i^{(\ell)} q_j^{(\ell)} + \sum_{i=1}^{n}\sum_{j=i}^{n}\sum_{m=j}^{n}\gamma_{ijm}^k q_i^{(\ell)} q_j^{(\ell)} q_m^{(\ell)}. \tag{21}$$

The previous system of equations for each $k \in [1, n]$ can be written in the matrix form as follows:

$$\begin{bmatrix} \mathbf{q}_\mathrm{quad}^T(\mathbf{q}^{(1)}) \\ \mathbf{q}_\mathrm{quad}^T(\mathbf{q}^{(2)}) \\ \vdots \\ \mathbf{q}_\mathrm{quad}^T(\mathbf{q}^{(n_\mathrm{L})}) \end{bmatrix} \begin{pmatrix} \beta_{11}^k \\ \beta_{12}^k \\ \vdots \\ \beta_{nn}^k \end{pmatrix} + \begin{bmatrix} \mathbf{q}_\mathrm{cub}^T(\mathbf{q}^{(1)}) \\ \mathbf{q}_\mathrm{cub}^T(\mathbf{q}^{(2)}) \\ \vdots \\ \mathbf{q}_\mathrm{cub}^T(\mathbf{q}^{(n_\mathrm{L})}) \end{bmatrix} \begin{pmatrix} \gamma_{111}^k \\ \gamma_{112}^k \\ \vdots \\ \gamma_{nnn}^k \end{pmatrix} \approx \begin{bmatrix} \mathbf{f}_\mathrm{nl}^T(\mathbf{u}_\mathrm{s}^{(1)}) \\ \mathbf{f}_\mathrm{nl}^T(\mathbf{u}_\mathrm{s}^{(2)}) \\ \vdots \\ \mathbf{f}_\mathrm{nl}^T(\mathbf{u}_\mathrm{s}^{(n_\mathrm{L})}) \end{bmatrix} \mathbf{V}_k \tag{22}$$

with:

$$\left\{\begin{array}{rcl} \mathbf{q}_{\text{quad}}(\mathbf{q}) & = & \begin{bmatrix}(q_1)^2 & q_1q_2 & q_2q_2 & q_2q_3 & q_3q_3 & \cdots & (q_n)^2\end{bmatrix}^T \\ \mathbf{q}_{\text{cub}}(\mathbf{q}) & = & \begin{bmatrix}(q_1)^3 & q_1q_1q_2 & q_1q_2q_2 & q_1q_2q_3 & q_1q_3q_3 & \cdots & (q_n)^3\end{bmatrix}^T. \end{array}\right. \tag{23}$$

With commercial FE softwares, the access to the source code is not granted and the coefficients have to be identified simultaneously by solving the system (22) that can be written as follows:

$$\begin{bmatrix}\mathbf{Q}_{\text{quad}} & \mathbf{Q}_{\text{cub}}\end{bmatrix}\begin{bmatrix}\boldsymbol{\beta}^k \\ \boldsymbol{\gamma}^k\end{bmatrix} \approx \begin{bmatrix} \mathbf{f}_{\text{nl}}^T(\mathbf{u}_{\text{s}}^{(1)}) \\ \vdots \\ \mathbf{f}_{\text{nl}}^T(\mathbf{u}_{\text{s}}^{(n_{\text{L}})}) \end{bmatrix}\mathbf{V}_k \tag{24}$$

For each k and $n \geq 3$, the system includes $n(n+1)/2$ unknowns for the coefficients β_{ij}^k and $(n^3+3n^2+2n)/6$ for the coefficients γ_{ijm}^k. The system is thus well determined when the number of loads n_{L} is equal to the number of coefficients; otherwise the system is over- or under-determined and a least square approximation is necessary. Note that when the problem presents symmetries, a significant number of coefficients are null and less load cases are required. When the quadratic and cubic coefficients cannot be computed separately, penalized regression methods such as Ridge, Lasso [44] or Elastic Net [45] can be preferred to the usual least-squares due to the possibly large condition number of the system.

The common approach is to identify the coefficients of the projected nonlinear forces via imposed displacements [41, 40, 37]. In the approach proposed in this paper, the loads and the associated solutions, computed to determine the dual modes, are reused here in the determination of the forces coefficients. Thus, no additional static computations are necessary.

3.3. Variant using the tangent stiffness matrix

When available as an output of the FE code, the use of the tangent stiffness matrix is suggested in [8] to compute the coefficients. Indeed, considering the Jacobian of the projected nonlinear forces, the system writes:

$$\begin{bmatrix} \delta\mathbf{Q}_{\text{quad}}(\mathbf{q}^{(1)}) \\ \delta\mathbf{Q}_{\text{quad}}(\mathbf{q}^{(2)}) \\ \vdots \\ \delta\mathbf{Q}_{\text{quad}}(\mathbf{q}^{(n_{\text{L}})}) \end{bmatrix} \begin{pmatrix} \beta_{11}^k \\ \beta_{12}^k \\ \vdots \\ \beta_{nn}^k \end{pmatrix} + \begin{bmatrix} \delta\mathbf{Q}_{\text{cub}}(\mathbf{q}^{(1)}) \\ \delta\mathbf{Q}_{\text{cub}}(\mathbf{q}^{(2)}) \\ \vdots \\ \delta\mathbf{Q}_{\text{cub}}(\mathbf{q}^{(n_{\text{L}})}) \end{bmatrix} \begin{pmatrix} \gamma_{111}^k \\ \gamma_{112}^k \\ \vdots \\ \gamma_{nnn}^k \end{pmatrix} \approx \begin{bmatrix} \widetilde{\mathbf{K}}_{\text{nl},k}^{(1)} \\ \widetilde{\mathbf{K}}_{\text{nl},k}^{(2)} \\ \vdots \\ \widetilde{\mathbf{K}}_{\text{nl},k}^{(n_{\text{L}})} \end{bmatrix}, \quad (25)$$

where

$$\delta\mathbf{Q}_{\text{quad}}(\mathbf{q}) = \begin{bmatrix} \dfrac{\partial\mathbf{q}_{\text{quad}}(\mathbf{q})}{\partial q_1} \\ \vdots \\ \dfrac{\partial\mathbf{q}_{\text{quad}}(\mathbf{q})}{\partial q_n} \end{bmatrix}, \quad \delta\mathbf{Q}_{\text{cub}}(\mathbf{q}) = \begin{bmatrix} \dfrac{\partial\mathbf{q}_{\text{cub}}(\mathbf{q})}{\partial q_1} \\ \vdots \\ \dfrac{\partial\mathbf{q}_{\text{cub}}(\mathbf{q})}{\partial q_n} \end{bmatrix}, \quad (26)$$

and where the notation $\widetilde{\mathbf{K}}_{\text{nl},k}^{(\ell)}$ corresponds to the transpose of the k^{th} row of the matrix $\mathbf{K}_{\text{nl}}^{(\ell)} = \mathbf{V}^T\mathbf{K}_{\text{nl}}(\mathbf{u}_{\text{s}}^{(\ell)})\mathbf{V}$.

As in the case with the nonlinear forces $\mathbf{f}_{\text{nl}}$, when the quadratic and cubic components of $\mathbf{K}_{\text{nl}}$ can be treated separately, the nonlinear coefficients $\boldsymbol{\beta}^k$ and $\boldsymbol{\gamma}^k$ can be identified individually by solving two different systems, otherwise the full system can be solved.

In [8], the tangent stiffness matrix is evaluated with imposed displacements. Here, the tangent stiffness matrix $\mathbf{K}_{\text{nl}}(\mathbf{u}_{\text{s}}^{(\ell)})$ is evaluated for the nonlinear static solutions $\mathbf{u}^{(\ell)}$ ($\ell \in [1, n_{\text{L}}]$) computed under the loads $\mathbf{f}_{\text{ext}}^{(\ell)}$. Each nonlinear static solution $\mathbf{u}^{(\ell)}$ gives a set of n equations, compared to only one equation with the nonlinear force $\mathbf{f}_{\text{nl}}(\mathbf{u}^{(\ell)})$. Thus, the number of static solutions necessary to compute the coefficients is much lower than with the method based on nonlinear forces in section 3.2.

Once the reduction basis and the coefficients of the nonlinear internal forces have been calculated, the coupling between this ROM and a fluid solver can be performed. The fluid-structure coupling procedure used in this work is discussed in the next section.

4. Partitioned fluid-structure coupling procedure between the fluid solver and the structural ROM

One application considered at the end of this paper is the simulation of the aeroelastic coupling between a structure undergoing large displacements induced by an aerodynamic loading. This coupling is addressed with a partitioned approach where the structural dynamics and the fluid dynamics equations are solved separately. Aerodynamics loads induced by the flow and structural displacements resulting from the deformable structure are exchanged at each physical iteration during the time integration. The loads corresponding to the structural displacements are balanced for each physical iteration with a fixed-point algorithm involving several sub-iterations. The flowchart Fig. 1 illustrates the time marching partitioned algorithm with the physical time loop and the fixed point loop introduced to converge the coupled aeroelastic state.

In this procedure, the structure that is usually represented by a set of linear modes in aeroelastic problems is replaced in the present case by the nonlinear ROM formulation introduced in the previous section 3 to take into account large displacements effects.

The flow is modeled here by the Navier-Stokes equations formulated in the Arbitrary Lagrangian-Eulerian framework [46] which is adapted to account for arbitrary grid motions, including both rigid body motions and deformations. The fluid equations are solved with the CFD Finite Volume solver elsA (ONERA-Safran property, [47]) under the following form for the conservative variables $\mathbf{w}$ on the entrained and deformable computation domain $\Omega(t)$ delimited by the boundary $\partial\Omega$ with unit external normal $\boldsymbol{n}(t)$:

$$\frac{\mathrm{d}}{\mathrm{d}t}\int_{\Omega(t)} \mathbf{w}\mathrm{d}\Omega + \int_{\partial\Omega(t)} \mathbf{F_c}[\mathbf{w}, \boldsymbol{s}]\boldsymbol{n}\mathrm{d}\Sigma + \int_{\partial\Omega(t)} \mathbf{F_d}[\mathbf{w}, \mathbf{gradw}]\boldsymbol{n}\mathrm{d}\Sigma = \mathbf{0} \quad (27)$$

with $\mathbf{F_c}$ (resp. $\mathbf{F_d}$) the convective (resp. diffusive) fluxes operators. The ALE formulation introduces the grid velocity term $\boldsymbol{s}(t)$ in the convective fluxes, which arises from the structural deformations at the fluid-structure interface. For viscous flow, the no-slip boundary condition imposes the continuity of the velocity at the fluid-structure interface Γ such that $\boldsymbol{v} = \boldsymbol{s}_\Gamma$ with $\boldsymbol{v}$ the flow velocity and $\boldsymbol{s}_\Gamma$ the velocity of the deformable fluid-structure interface.

This grid velocity at the interface $\boldsymbol{s}_\Gamma = \mathbf{u}_\Gamma = \mathbf{V}_\Gamma\dot{\mathbf{q}}$ is the time derivative of the structural deformation which is decomposed here on the restriction of the reduced basis $\mathbf{V}_\Gamma$ on the fluid-structure interface.

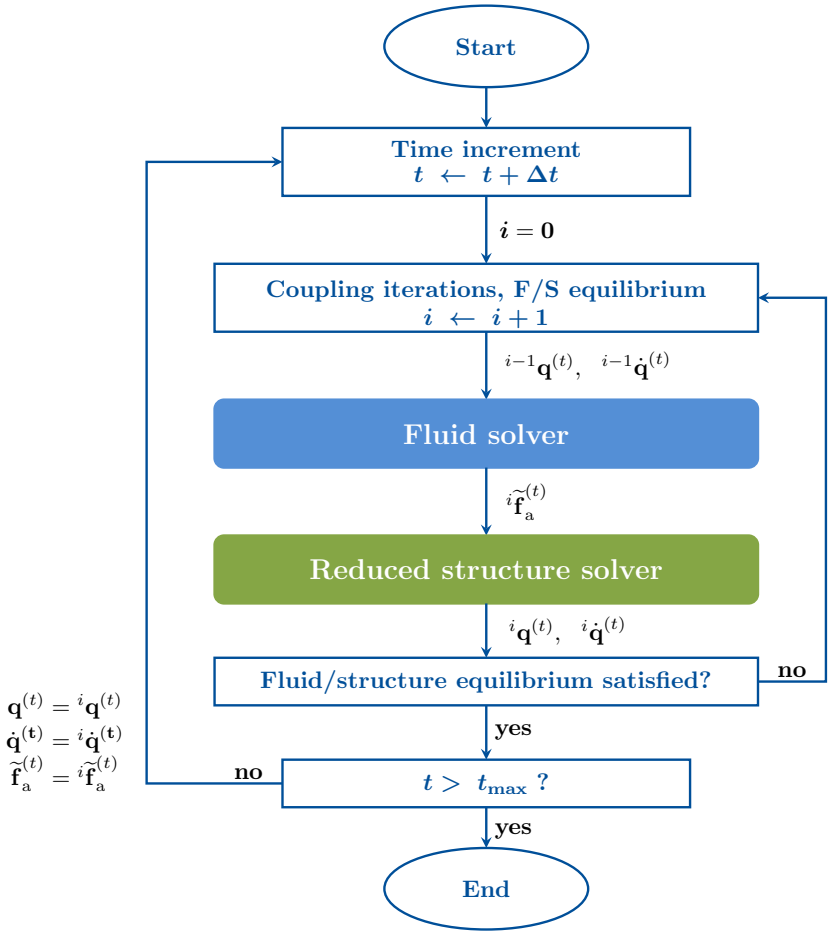

Figure 1: Partitioned coupling procedure between the fluid solver and the nonlinear reduced structural solver. The projection of the aerodynamics forces in the reduced basis is denoted here by $\widetilde{\mathbf{f}}_{\mathrm{a}} = \mathbf{V}^T \mathbf{f}_{\mathrm{a}}$.

The structural deformation at the interface $\mathbf{u}_\Gamma$ has to be propagated inside the fluid computational domain to accommodate with the deformed position of the interface. The fluid mesh coordinates are denoted $\boldsymbol{\xi} = [\boldsymbol{\xi}_{\mathrm{i}}, \boldsymbol{\xi}_\Gamma]$ with $\boldsymbol{\xi}_{\mathrm{i}}$ the internal grid coordinates and $\boldsymbol{\xi}_\Gamma$ the fluid mesh coordinates on Γ. These latter satisfy $\boldsymbol{\xi}_\Gamma = \mathbf{u}_\Gamma$ and a mesh deformation algorithm based on a structural analogy is exploited to propagate the deformation in the whole fluid domain [48]. The fluid domain is assimilated to a linear elastic material where prescribed displacements are imposed on the interface Γ. The problem is formulated with a classical FE formulation as $\mathbf{K}_{\mathrm{mesh}}\boldsymbol{\xi} = \mathbf{0}$ in Ω with $\mathbf{K}_{\mathrm{mesh}}$

a stiffness matrix resulting from the assembly of all the local stiffness matrices per element and the constraint $\boldsymbol{\xi}_\Gamma = \mathbf{u}_\Gamma$. The Young's modulus considered to build the stiffness matrix is however not uniform in the fluid domain but depends on the mesh metrics. The finite element problem is decomposed as:

$$\begin{bmatrix} \mathbf{K}^{\mathrm{ii}}_{\mathrm{mesh}} & \mathbf{K}^{\mathrm{i}\Gamma}_{\mathrm{mesh}} \\ \mathbf{K}^{\Gamma\mathrm{i}}_{\mathrm{mesh}} & \mathbf{K}^{\Gamma\Gamma}_{\mathrm{mesh}} \end{bmatrix} \begin{bmatrix} \boldsymbol{\xi}_{\mathrm{i}} \\ \boldsymbol{\xi}_\Gamma \end{bmatrix} = \begin{bmatrix} \mathbf{0} \\ \mathbf{R}_\Gamma \end{bmatrix} \tag{28}$$

with $\mathbf{R}_\Gamma$ the reaction on the fluid-structure interface Γ. Therefore, internal displacements of the fluid mesh $\boldsymbol{\xi}_{\mathrm{i}}$ are obtained as the solution of the linear problem:

$$\mathbf{K}^{\mathrm{ii}}_{\mathrm{mesh}} \boldsymbol{\xi}_{\mathrm{i}} = -\mathbf{K}^{\mathrm{i}\Gamma}_{\mathrm{mesh}} \boldsymbol{\xi}_\Gamma \tag{29}$$

Since a modal approach is considered in the present work, a collection of fluid mesh deformation fields can be computed during a pre-processing step by prescribing at the fluid structure interface the modal deformation $\boldsymbol{\xi}_\Gamma = \mathbf{v}_\Gamma$ for each basis vector $\mathbf{v}$ of the reduction basis $\mathbf{V}$. The grid velocity $\boldsymbol{s}$ involved in the convective fluxes is finally evaluated from the time derivative of the fluid mesh grid position updated at each iteration by the mesh deformation procedure. In the general case, the fluid and structural mesh discretization are non-coincident and an additional step is necessary to transfer on one hand the structural displacements from the structural mesh to the aerodynamic one, and on the other hand the aerodynamic loads computed on the fluid cells interfaces to the structural nodes.

When the fluid and structure meshes are non-coincident, a step of transfer of the structural displacements to the fluid boundary is necessary. Likewise, the fluid aerodynamic forces have to be transferred to the structure. This transfer is performed here by a reconstruction of the displacement field on the beam's external cross section from the degrees of freedom known on the beam's neutral axis.

In what follows, the reduced-order models presented previously are applied to the 2D case of a von Kármán beam in section 5. Firstly, the behavior of the structure under different load types is investigated. Then, the ability of the ROM to capture an aeroelastic coupling is investigated in section 6.

5. Application to a nonlinear beam

5.1. FE Euler-Bernoulli beam with von Kármán hypothesis

In this section, a Euler-Bernoulli beam model is considered, the shear deformation of the sections is thus neglected. In each element of the discretized beam, the von Kármán hypothesis of moderate rotations is assumed. With such a model, the curvature κ and the engineering strain e are given by

$$\kappa = \frac{\partial \theta}{\partial X} = \frac{\partial^2 v}{\partial X^2}, \tag{30}$$

$$e = \frac{\partial u}{\partial X} + \frac{1}{2}\left(\frac{\partial v}{\partial X}\right)^2, \tag{31}$$

where u, v, θ are respectively the axial, vertical displacements and the rotation of the section, represented in Figure 2.

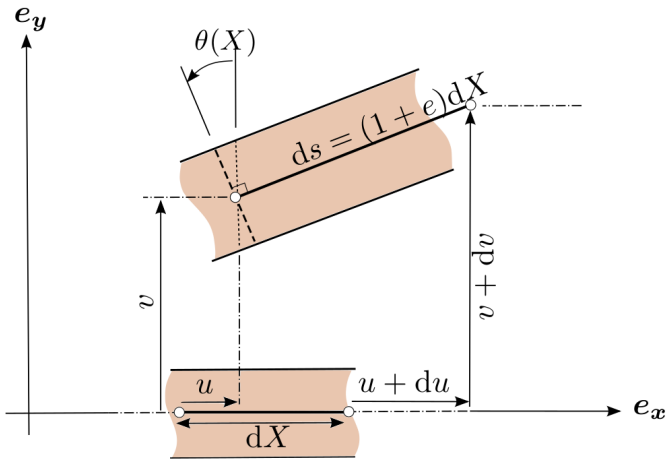

Figure 2: Definition of the engineering strain

The FE discretization of Euler-Bernoulli beams is based on linear shape functions for the axial degrees of freedom and cubic Hermitian shape functions for the vertical and rotation degrees of freedom. More details are provided in appendix A. With the von Kármán hypothesis, membrane-locking issues may appear, especially for a free boundary condition [49]. Indeed, at a free end (here at $x = L$ for a cantilever beam), the membrane strain is null for any position X in the last element:

$$e = 0 = \frac{\partial u}{\partial X} + \frac{1}{2}\left(\frac{\partial v}{\partial X}\right)^2. \tag{32}$$

It means that the degree of the polynomial of $\partial u/\partial X$ and $(\partial v/\partial X)^2$ has to be the same. However, the shape functions for u are linear and those for v are cubic. Therefore, the above-mentioned constraint is not satisfied and leads to excessively stiff elements. This membrane-locking phenomenon is significantly accentuated when the lengths of the discretization elements are large. In order to circumvent membrane-locking, a reduced integration of the nonlinear terms with only one Gauss point is used, as suggested in [49].

A clamped-free beam of rectangular cross-section is considered for the application. The beam is discretized with 50 elements in which the von Kármán hypothesis is considered. The dimensions and properties of the beam are presented in Table 1.

Beam dimensions	
L (length)	4 m
h (thickness)	7.10^{-2} m
b (width)	$3h$

Material properties	
E	100 GPa
ρ	4400 kg.m^{-3}

Table 1: Dimensions and material properties of the beam

It is well known that the Euler-Bernoulli beam model with von Kármán hypothesis has a limited range of validity, as shown for example in [30]. Indeed, for cantilever beam under external loads with no axial contribution, the geometric nonlinearity cancels out in the vertical and rotational components, leading to purely axial nonlinearity. However, we have chosen to use this model because geometric nonlinearities in such a case are cubic in the degrees of freedom. The proposed ROM is therefore directly transposable to 3D finite element applications with Saint Venant-Kirchhoff model where the geometric nonlinearity is known to be cubic in the degrees of freedom.

5.2. Reduced-order beam model with dual modes

The first three linear normal modes are initially considered in order to build the reduction basis. Those modes are bending modes that do not capture the membrane dynamics. As explained in the previous section, the basis is completed with dual modes determined by imposing loads to the structure, with the distribution defined in Eq.(6) as the combination of the first three linear modes:

$$\mathbf{f}_{\text{ext}}^{(\ell)} = \mathbf{K}\Big(\pm \alpha_1^{(\ell)}\boldsymbol{\phi}_1 \pm \alpha_2^{(\ell)}\boldsymbol{\phi}_2 \pm \alpha_3^{(\ell)}\boldsymbol{\phi}_3 \Big), \tag{33}$$

with the modes $\boldsymbol{\phi}_1, \boldsymbol{\phi}_2, \boldsymbol{\phi}_3$ normalized by their maximal vertical value and $\alpha_1^{(\ell)} \in \{10h, 0\}$, $\alpha_2^{(\ell)} \in \{1h, 0\}$, $\alpha_3^{(\ell)} \in \{1h, 0\}$. With this choice of amplitudes $\alpha_i^{(\ell)}$, the first linear mode is considered as a dominant mode undergoing large deformations and slightly perturbed in the direction of the other linear normal modes. The loads are imposed positively and negatively so that no side is favored in the construction of the database of nonlinear static solutions for the $n_{\mathrm{L}} = 26$ different load cases. A singular value decomposition of the static resolution remainders is then performed according to the process of selection of the dual modes detailed in section 3.1. The singular values and the linearized strain energies of the dual modes candidates are plotted in Figure 3.

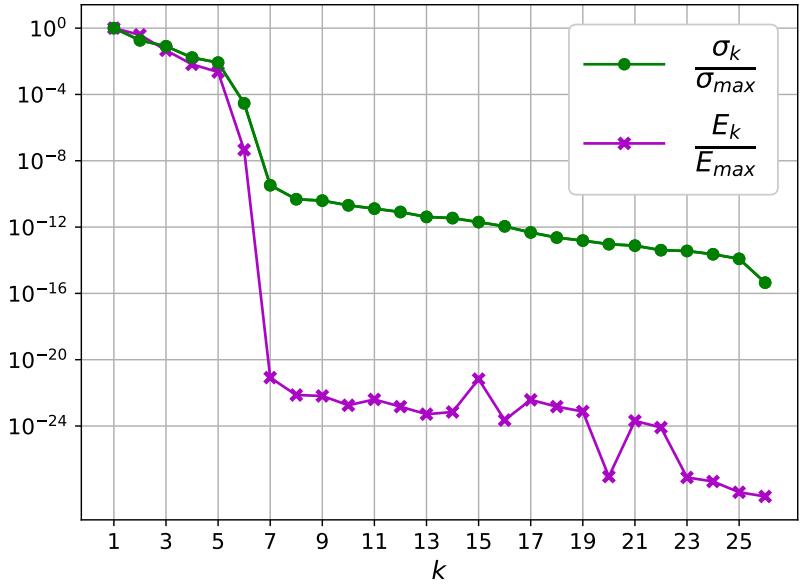

Figure 3: Singular values and linearized strain energies of the static solution remainders.

In the present case, the SVD modes with the highest singular values are also those with the highest linearized strain energy contribution. The dual modes appended to the initial basis of linear modes are thus the vectors $\mathbf{d}_{\{1,2,3,4,5\}}$. In cases such as the present configuration, it could be argued that only the criterion of the singular values can be retained. However, the criterion based on the energy highlights, among the dual modes candidates with large singular value, those with a significant membrane contribution.

When there is no clear drop in the singular values, it was observed on other configurations that some dual modes candidates with a small contribution to the linearized energy may contribute less to the dynamics and are not necessary in the reduction basis. The new reduction basis considered is therefore the concatenation of the first 3 linear normal modes and the 5 dual modes: $\mathbf{V} = [\mathbf{\Phi}, \mathbf{d}_{\{1,2,3,4,5\}}]$. It is worth mentioning that for beam applications, the dual modes leading to a high linearized strain energy have a negligible bending contribution compared to their axial contribution. Indeed, the axial stiffness of a beam is larger than the bending stiffness. Thus, the linearized strain energy associated to vectors with dominant membrane contribution is usually larger than the one of modes with dominant bending contribution. With this selection of dual modes, the relative error in precision defined in Eq.(17) is $\varepsilon_\sigma = \mathcal{O}(10^{-6})$ and the relative error in linearized strain energy contribution defined in Eq.(18) is $\varepsilon_E = \mathcal{O}(10^{-8})$.

The reduction basis $\mathbf{V}$ obtained, the next step in the construction of the model is the determination of the projected nonlinear forces from the expression (21). The coefficients of the polynomial are identified with the *Implicit Condensation* method by imposing load cases defined as in Eq.(11). The loads and associated nonlinear static solutions defined previously for the dual modes selection are reused here. Besides, due to symmetry considerations on the geometry and the linear normal modes, many nonlinear coefficients are null. Some coefficients are also null because the dual modes have only axial contributions, leading to null coefficients in the expression of the internal forces for the von Kármán beam (detailed in Appendix A). Since the expression of the nonlinear forces $\mathbf{f}_{\text{nl}}$ is explicitly known for our beam problem, the internal nonlinear forces can be decomposed in their quadratic $\mathbf{f}_{\text{nl}}^{\text{quad}}$ and their cubic $\mathbf{f}_{\text{nl}}^{\text{cub}}$ contributions (cf. Appendix A). The quadratic and cubic coefficients introduced in Eq.(22) can therefore be split in two different matrices. The nonlinear force coefficients are then identified from two independent systems which are better conditioned when considered separately. It has been verified on this test case, that the nonlinear coefficients obtained using the nonlinear forces as well as those using the tangent stiffness matrices (method detailed in section 3.3) match exactly with a symbolic computation of the coefficients. A method based on imposed displacements [35, 8] also resulted in the same coefficients.

In the rest of the paper, the *Implicit Condensation* method with dual modes will be called ICDual, to differentiate the method from the classical IC method with only bending modes and from the ICE method.

5.3. Structural response under different load cases

In this section, the efficiency of the ROM will be evaluated on two different load cases illustrated in Figure 4: a vertically distributed load along the beam and a following load at the tip. The ICDual ROM will be compared to the ICE solution and the solution obtained with the nonlinear full-order model (FOM), firstly on a static load case, then under a dynamic load case at the resonance of the first linear normal mode.

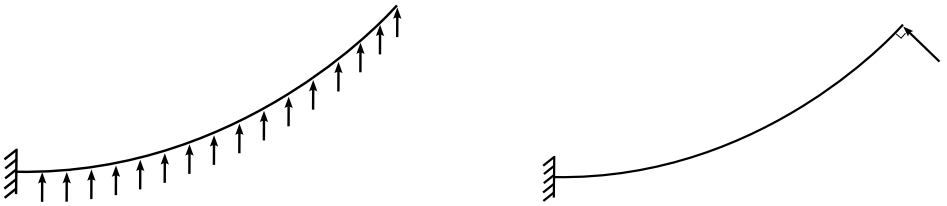

Figure 4: Load cases considered: (a) Distributed vertical load; (b) Follower load at tip

5.3.1. Load case 1: Vertical distributed load along the beam

The first loading case consists of a vertical uniformly distributed load on the beam. The total load applied to the beam is $80,000$ N, meaning a uniformly distributed load density of $20,000$ N/m. The geometric nonlinearity alters the vertical amplitude of the displacement and produces a significant axial shortening due to the coupling between the axial and vertical displacements. On the contrary, the linear computation does not lead to any axial shortening since bending and traction-compression are not coupled.

The classical *Implicit Condensation* method (IC) and its *Expansion* (ICE) are compared to the ICDual ROM and the linear and nonlinear reference solutions in Figure 5. Regarding the IC/ICE ROMs, the first 3 linear normal modes are used in the reduction basis. The vertical displacement of the beam is well captured by the IC method. However, the axial displacement is not captured at all. The reason is that the reduction basis contains only bending modes, thus no equation solves the axial displacement in the reduced system. Nonetheless, the *Expansion* step (ICE) enables to rebuild the axial displacement in post-processing and matches with the FOM solution. With the ICE method, the nonlinear static solution was obtained with only 3 linear normal modes. The solution is first computed with the IC method and then post-processed with the *Expansion* step. The ICE method is very accurate on this static case since the reconstruction step of the Expansion phase is

based on a static correction which is adapted here to capture the missing membrane effect.

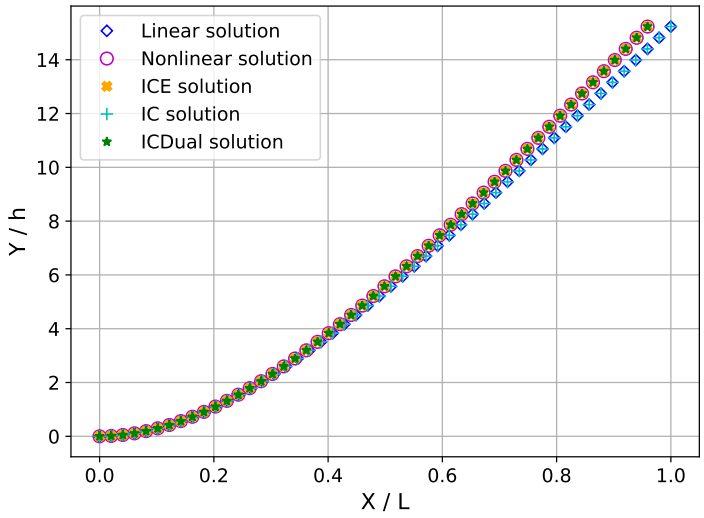

(a) Beam deformation

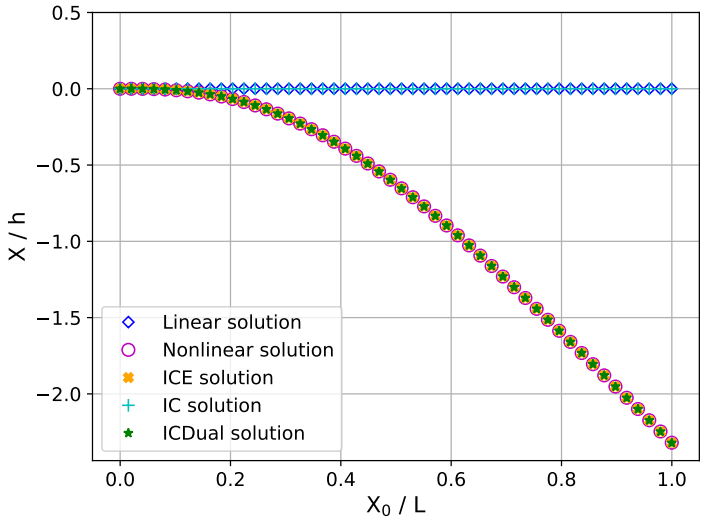

(b) Axial displacement

Figure 5: Nonlinear static displacement of the clamped-free von Kármán beam, loaded with a vertical uniformly distributed load along the beam of $20,000$ N/m. Comparison between the linear FOM, nonlinear FOM, the IC/ICE and ICDual solutions.

The ICDual ROM contains the same linear bending modes as the ICE

method, completed with the five dual modes determined previously. Such a ROM perfectly captures the nonlinear FE solution as a result of the computation, while the same result was obtained with the ICE method only after the *Expansion* step.
Table 2 represents the relative cumulative error according to the axial u_i and vertical v_i degrees of freedom:

$$\varepsilon_{\text{cumul}} = \frac{\sum_{i=1}^{n_{\text{dof}}} \sqrt{(u_i - u_i^{\text{FOM}})^2 + (v_i - v_i^{\text{FOM}})^2}}{\sum_{i=1}^{n_{\text{dof}}} \sqrt{(u_i^{\text{FOM}})^2 + (v_i^{\text{FOM}})^2}} \tag{34}$$

Table 2: Error regarding the nonlinear FOM solution of the beam displacement for several amplitudes of static distributed load.

	Relative cumulative error $\varepsilon_{\text{cumul}}$ (%)		
Total load integrated (N)	$40,000$	$60,000$	$80,000$
Linear FOM	6.67	9.98	13.25
ICE ROM	2.276×10^{-2}	2.321×10^{-2}	2.377×10^{-2}
ICDual ROM	2.285×10^{-2}	2.338×10^{-2}	2.406×10^{-2}

The error is computed on the norm of the displacement. Since the ICE and ICDual ROMs are very close, the error component by component gives the same conclusions. This validates the approach followed here with a reduction basis enriched with dual modes in pre-processing. Nevertheless, the ICDual method solves the coupled dynamics of the system in bending and traction-compression, instead of restricting the dynamics to the bending and rebuilding the coupling with the ICE afterwards. This will be of paramount importance for the following dynamic application.

The ICDual method is now evaluated on a dynamic case and compared to the result of the ICE method. The load distribution is the same as the static case, but its amplitude is reduced to 1400 N/m to obtain displacements with the same order of magnitude as the fluid-structure interaction case of section 6.3. A sinusoidal time dependence is applied to the loading with a frequency $f_0 = 3.37$ Hz (frequency of the first mode). A Rayleigh damping $\mathbf{C} = 2\xi\omega_0\mathbf{M}$

is considered, with $\xi = 5 \times 10^{-2}$ and $\omega_0 = 2\pi f_0$ the pulsation of the first linear normal mode. Figure 6 displays the vertical and axial displacements at the tip of the beam once the periodic regime is established. The time integration is carried out using a classical nonlinear Newmark algorithm with Newton-Raphson iterations.

The vertical displacement plotted in Figure 6(a) is very close in terms of amplitude for both the ICE and the ICDual methods. There is however a slight phase shift of 9.70° between the reference nonlinear solution and the ICE and linear solutions.

Table 3: Relative error of the maximal displacement of the beam tip in periodic regime between the reference nonlinear FOM model and the linear FOM, ICE ROM and ICDual ROM models.

	Relative error of the tip displacement (%)	
	Y component	X component
Linear FOM	2.630	100
ICE ROM	2.630	5.176
ICDual ROM	2.023×10^{-4}	6.266×10^{-4}

Table 3 contains the relative axial ($|x_{\max} - x_{\max}^{\text{FOM}}|/|x_{\max}^{\text{FOM}}|$) and vertical ($|y_{\max} - y_{\max}^{\text{FOM}}|/|y_{\max}^{\text{FOM}}|$) errors of the maximal displacements of the beam tip in periodic regime between the reference nonlinear FOM model and the different models. The ICDual ROM captures perfectly the axial dynamics, both in terms of amplitude and phase (Figure 6(b)), whereas the ICE method is inaccurate. This results highlights the drawback of the ICE method where the dynamics of the system in traction-compression is not computed by the projected equation of the dynamics but rebuilt with limited information. Besides, the *Expansion* step of the ICE method is a static reconstruction which depends only on the generalized coordinates of the bending modes, not on the velocity or the acceleration. With the ICE method, the axial displacement is therefore governed only by the projection of the beam on the bending modes, whatever the dynamics of it, whether it is static, quasi-static or strongly dynamic. Moreover, increasing the number of modes in the reduction basis to 8 or 10 modes does not improve the axial ICE solution since the dynamics in traction-compression is missing in the reduced equation of the dynamics Eq.(2). On the contrary, with only 5 dual modes added to the

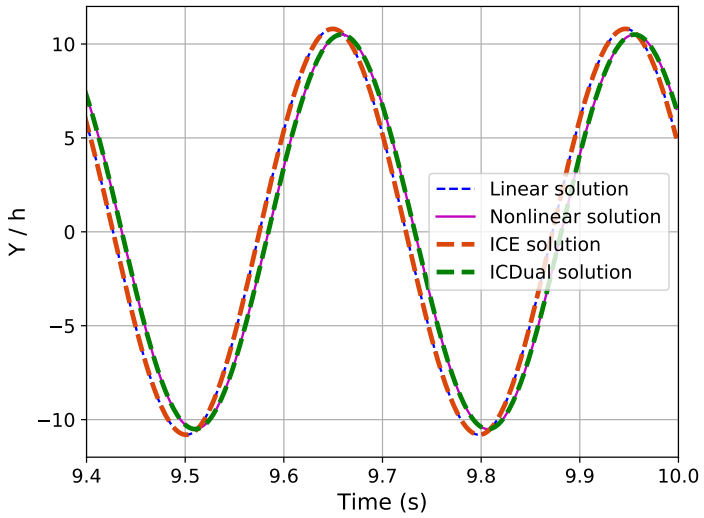

(a)

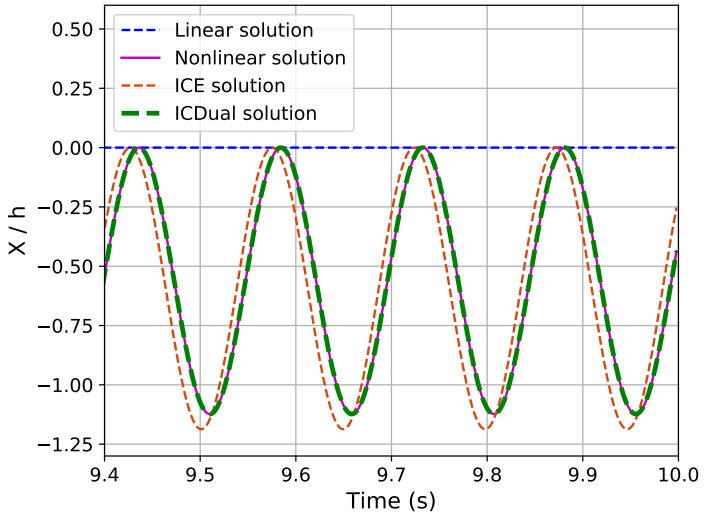

(b)

Figure 6: Nonlinear dynamic displacement of the clamped-free Euler-Bernoulli/von Kármán beam, loaded vertically with a uniformly distributed load of 1400 N/m and of frequency $f_0 = 3.37$Hz. The time step is 2×10^{-3}s and the structural damping $\mathbf{C} = 2\xi\omega_0\mathbf{M}$ with $\xi = 5 \times 10^{-2}$. Comparison of the vertical (a) and axial (b) displacements at the tip of the beam between the nonlinear FE solution, the ICE and the ICDual computations.

reduction basis, the dynamics, both in traction-compression and in bending is perfectly captured.

5.3.2. Load case 2: Follower force at the tip

The second load case considered is a concentrated follower load applied at the tip of the beam. In this case, the solution is inherently nonlinear since the external loads depends on the beam's position which undergoes large nonlinear displacements. The amplitude of the load equal to $30,000$ N. Figure 7 represents the classical IC and ICE solutions compared to the ICDual solution. Contrary to the previous static load case, the ICE solution no longer matches the nonlinear reference solution. Indeed, the projection of the follower force on the reduction basis filters out the axial components since the basis includes only bending modes with vertical contributions. Finally, the ICE method behaves as if the external load case was a purely vertical load since the *Expansion* step is not able to retrieve a correction adapted to the follower load. Increasing the number of linear normal modes in the reduction basis for the ICE method to 8 and even 10 did not improve the solution since the additional modes are still bending modes. The solution may be improved by introducing membrane modes, or, as suggested in the literature, to treat follower forces as an extension of the ICE method [28].

Unlike the ICE solution, the ICDual ROM perfectly captures the nonlinear FOM solution as shown in Figure 7 and its precision is quantified in Table 4. Indeed, with the dual modes in the reduction basis, the external forces are well represented in the reduction basis and the solution of the reduced system gives the correct nonlinear static solution.

Table 4: Error regarding the nonlinear FOM solution of the beam displacement for several amplitudes of static follower load at tip.

	Relative cumulative error $\varepsilon_{\text{cumul}}$ (%)		
Load (N)	$10,000$	$20,000$	$30,000$
ICE ROM	1.25	4.91	10.60
ICDual ROM	1.039×10^{-1}	1.288×10^{-1}	2.814×10^{-1}

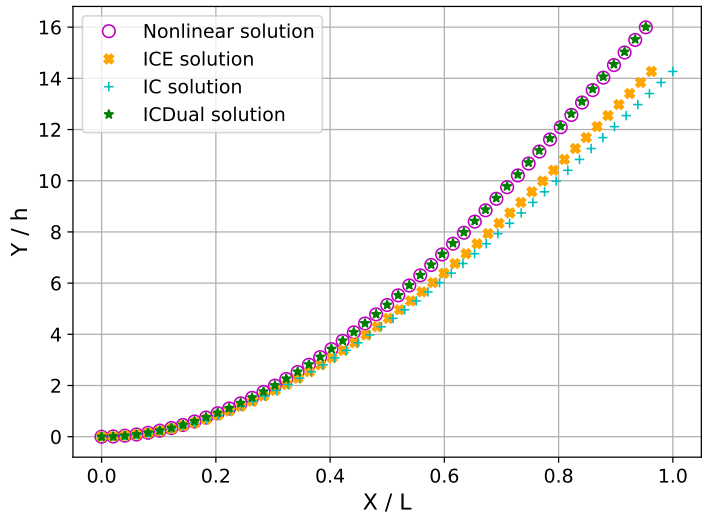

(a) Beam deformation

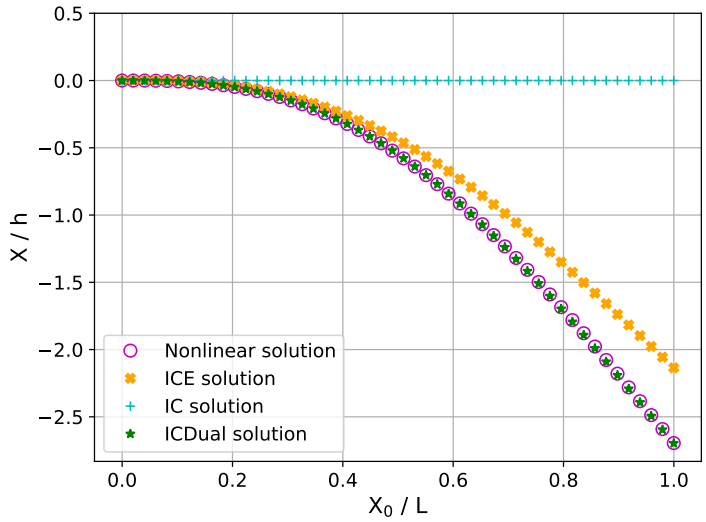

(b) Axial displacement

Figure 7: Nonlinear static displacement of the clamped-free Bernoullli/von Kármán beam, loaded at the tip with a follower load 30, 000 N. Comparison between the nonlinear, the IC, ICE and ICDual solutions.

The dynamics of the structure is then studied with a sinusoidal follower load, with the same frequency as the previous load case and an amplitude of

2500 N. The Rayleigh damping and time step are also unchanged from the previous test case. Figure 8 shows the evolution in the periodic regime of the axial displacement at the tip of the beam and Table 5 summarizes the relative errors of the models compared to the nonlinear FOM solution.

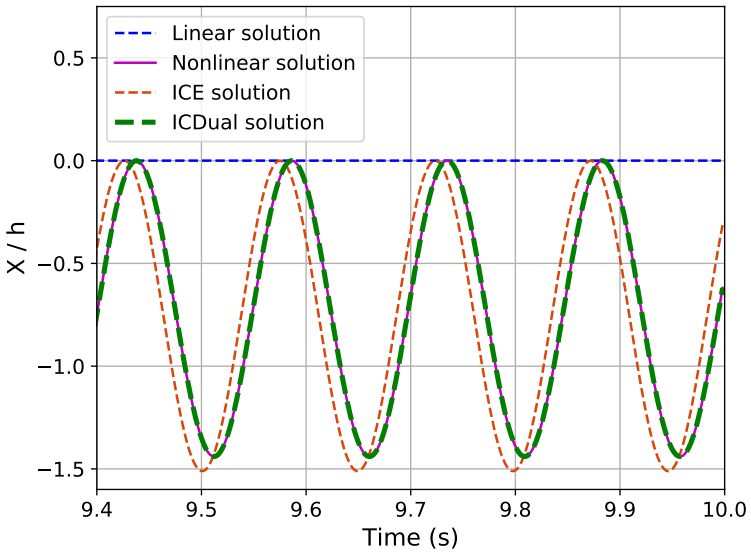

Figure 8: Nonlinear dynamic displacement of the clamped-free Euler-Bernoulli/von Kármán beam loaded at the tip with a dynamic follower load of amplitude 2500 N and of frequency $f_0 = 3.37$ Hz. The time step is 2×10^{-3}s and the structural damping $\mathbf{C} = 2\xi\omega_0\mathbf{M}$ with $\xi = 5 \times 10^{-2}$. Comparison of the axial displacement at the tip of the beam between the nonlinear FE solution, the ICE and the ICDual computations.

The ICDual solution matches the FOM solution like for the other test case, while the ICE solution presents a phase shift of 12° and does not render the axial displacement accurately. Other test cases were also tested such as a purely vertical load at the tip and a follower distributed load. The results under such load cases are not presented here for the sake of brevity but the same conclusions were obtained. Both the ICE and ICDual ROMs were accurate for the static vertical load at the tip but only the ICDual ROM was accurate in the dynamic case. Regarding the distributed follower load, only the ICDual ROM was accurate for both the static and dynamic cases.

In this section, the ICDual ROM was built for a Euler-Bernoulli/von Kármán beam and compared on different load configurations to solutions obtained with the IC and ICE methods. In all cases, both the static and

Table 5: Relative error of the maximal displacement of the beam tip in periodic regime between the reference nonlinear FOM model and the ICE and ICDual ROM models.

	Relative error of the tip displacement (%)	
	Y component	X component
ICE ROM	2.472	4.919
ICDual ROM	3.643×10^{-3}	8.175×10^{-3}

dynamic nonlinear responses were precisely captured. The limitations of the classical ICE method have been highlighted, especially when dealing with follower forces or dynamic loads. Since the dual modes added in the reduction basis have only membrane contribution, it could be argued that linear membrane modes could be used instead. However, to obtain similar results with pure membrane modes it is necessary to include all the membrane modes. This would lead to a tremendous number of coefficients ($\mathcal{O}(10^5)$) to identify for the additional 49 membrane modes, whereas similar results are obtained with only 5 dual modes. It is worth mentioning that the ICDual ROM has also been tested by the authors on the clamped-clamped beam configuration subjected to static and dynamic loads. The results are not presented in this paper for the sake of brevity but it was observed that the ICDual ROM also matches perfectly with the full order solutions.

6. Application to a fluid-structure interaction test case

In this part, the efficiency of the reduced-order model is investigated on a fluid-structure interaction problem where the flexible beam is placed in the wake of a circular cylinder. The external forces are aerodynamic forces, distributed on the beam and resulting from the vortices shed in the wake of a fixed cylinder. The interaction between the flexible beam and the vortices will lead to the vibration of the beam.

6.1. Numerical setup

The boundary conditions of the test case are depicted in Figure 9. A no-slip adiabatic wall condition is imposed to the fluid on the surface of the fixed cylinder and of the flexible beam. Non-reflecting boundary conditions with a constant axial velocity are imposed at the inlet and outlet borders. This condition is based on the characteristic relations and prevents unsteady waves to be reflected in a non-physical fashion. The upper and lower boundary conditions are chosen far enough from the structure in order to avoid confinement effects that would impact the vortex shedding behind the cylinder. Slip boundary conditions are imposed at those walls unlike in [50] where no slip boundary conditions are applied. With upper and lower slip boundary conditions, the case without the beam placed behind the cylinder which is first considered in section 6.2, produces the classical Von Karman vortex street. The Strouhal number associated to this vortex shedding will be compared to validate the test case.

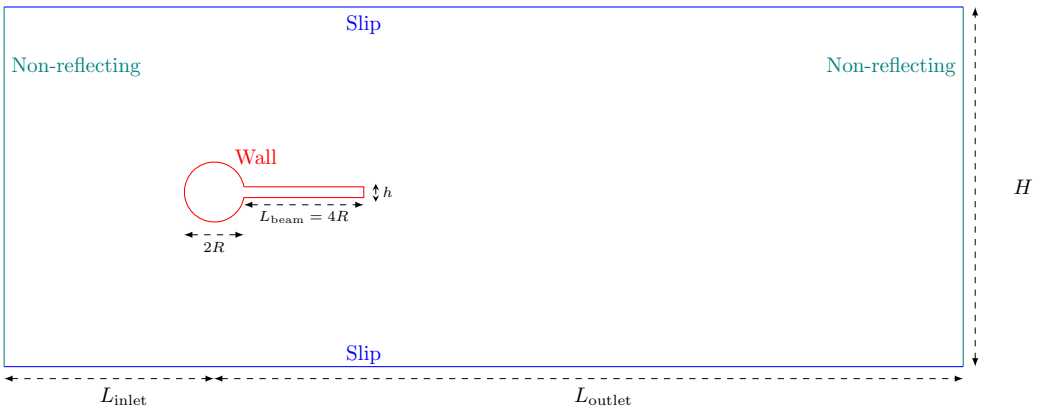

Figure 9: Computational domain and boundary condition of the fluid-structure interaction test case.

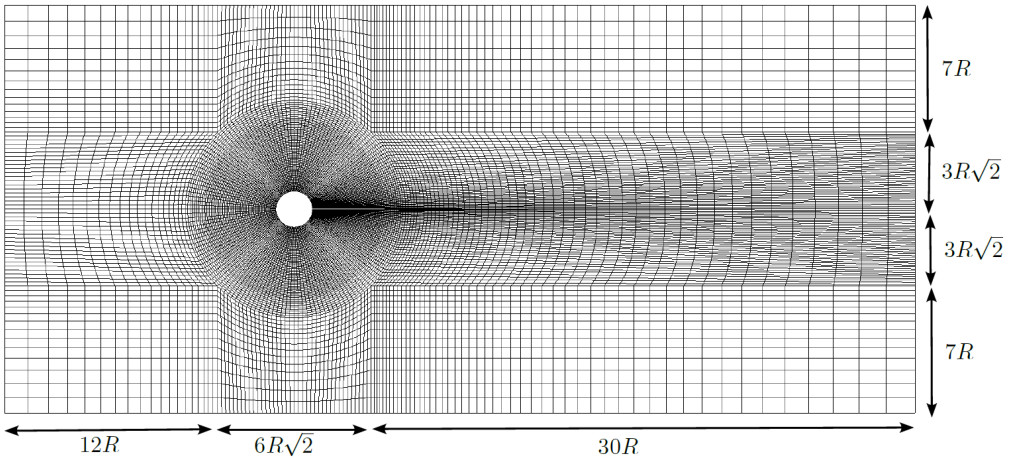

Figure 10: Mesh and dimensions of the fluid domain around the cylinder and the beam.

The structured fluid mesh is refined around the structure and in the near wake (Figures 10, 11), and is then progressively coarsened from the structure to the external domain boundaries.

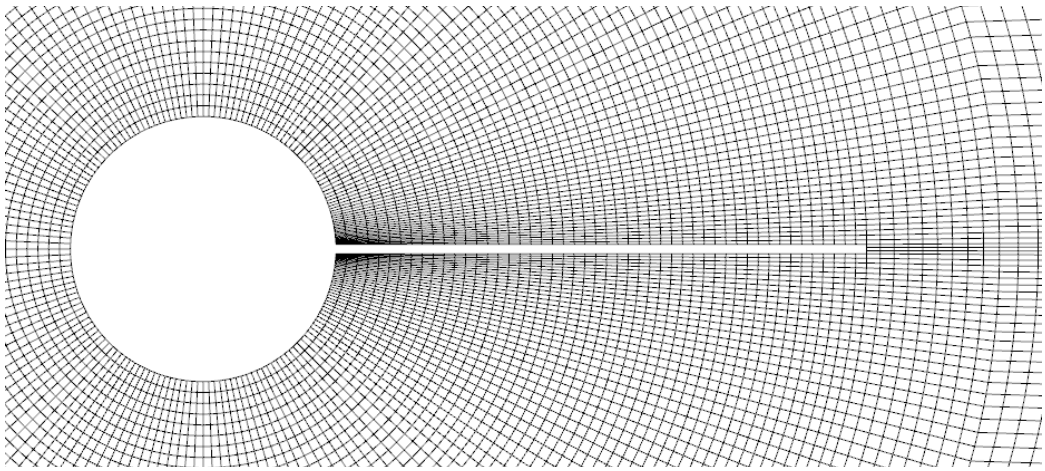

Figure 11: Focus of the mesh in the close vicinity of the cylinder and the beam. The beam thickness is discretized with 3 Finite Volumes cells.

The fluid is solved with the Finite Volume CFD software *elsA* [47] (ONERA-Safran property). The fluid is a diatomic gas, following the perfect gas equations whose properties are detailed in Table 6.

Physical quantity	Value
T_∞	300 K
p_∞	101,325 Pa
γ	1.4
R_{specific}	287.053 J.kg^{-1}.K^{-1}
$c_v = \frac{5}{2} R_{\text{specific}}$	717 J.kg^{-1}.K^{-1}

Table 6: Fluid properties for the flow around the cylinder.

The fluid density is deduced from the perfect gas equation:

$$\rho_\infty = \frac{p_\infty}{R_{\text{specific}}\, T_\infty} = 1.17 \text{ kg.m}^{-3}. \tag{35}$$

The viscosity μ_∞ is set to 0.4 Pa.s to have the targeted Reynolds number with a reasonable inlet velocity (equivalent to Mach number 0.1) and a given diameter D:

$$Re = \frac{\rho_\infty U_\infty D}{\mu_\infty} = 200. \tag{36}$$

The convective fluxes are approximated by the AUSM+ (P) MiLES scheme [51], [52] to benefit from its low dissipation property and its ability to model low-Mach boundary layer flows. The time step for unsteady simulations is $dt = 4.11 \times 10^{-3}$ s.

6.2. Von Kármán vortices in the wake of the cylinder without beam

In this part, we consider only the fixed cylinder, without the beam. As illustrated by Figure 12, a typical von Kármán vortex street develops in the wake of the cylinder.

The dimensionless Strouhal number defined below characterizes the flow periodicity based on the vortex shedding frequency F_s, the characteristic length (diameter cylinder D) and the inflow velocity U_∞ as :

$$St = \frac{F_s D}{U_\infty}. \tag{37}$$

For the flow around the cylinder, the Strouhal number can be evaluated by the relation $St = 0.212 - 2.7/Re$ proposed by Roshko [53] based on experimental data in the range $200 \leq Re \leq 2,000$.

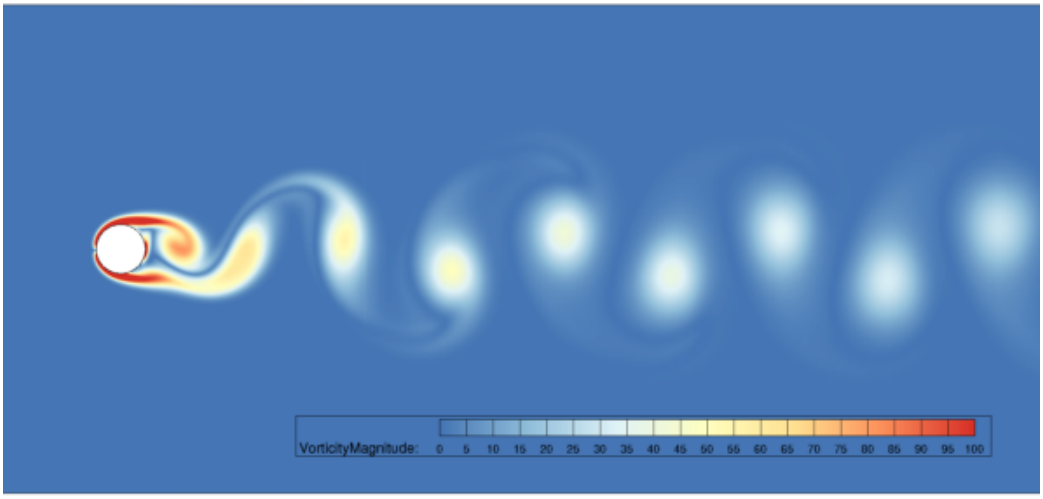

Figure 12: Von Kármán vortices in the wake of the fixed cylinder. Visualization of the vorticity magnitude.

Figures 13a and 13b represent respectively the drag and lift forces that the cylinder undergoes. The periodic oscillations of the vortex emissions can be observed in those figures. For each oscillation of the lift force F_y, two counter-rotating vortices are shed. Thus the oscillation frequency of the drag force F_x is twice the oscillation frequency of F_y. With the shedding frequency $F_s = 3.42$ Hz evaluated from the lift force, the Strouhal number obtained with the present simulation is St $= 0.197$ which is very close to the value $St = 0.212 - 2.7/Re = 0.198$ provided by Roshko's relation for Re $=$ 200. This validates the numerical fluid model which is then extended in the next section to a fluid-structure interaction case.

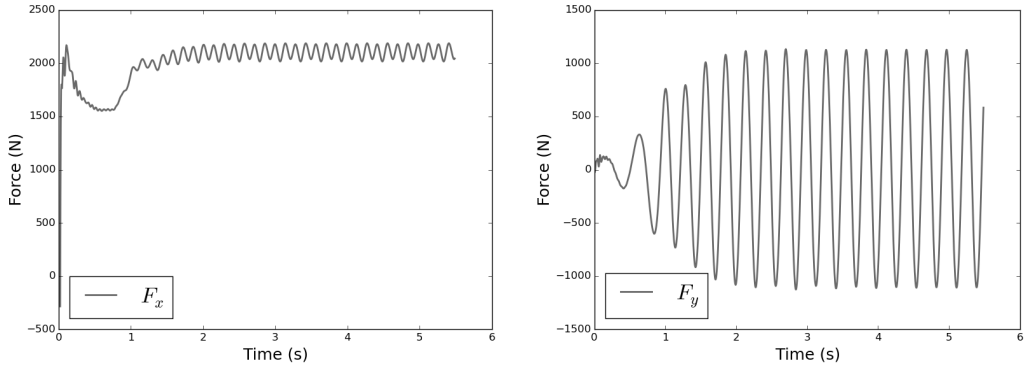

(a) Drag force F_x

(b) Lift force F_y

Figure 13: Aerodynamic drag (a) and lift (b) forces on the cylinder resulting from the vortex shedding in the wake.

6.3. Fluid-structure interaction between the a flexible beam and the wake of the cylinder

The flexible beam studied in section 5 is now placed in the wake of the fixed cylinder. The movement of a flexible beam triggered by the vortices has already been studied in [50, 54] on a similar type of test case. The displacements on the beam's wet surface are interpolated from the displacements and rotations of the middle line. The axial discretization of the beam is the same as in section 5.3 and coincides with the axial local fluid mesh at the skin of the beam. As a result, no specific load transfer method is needed to propagate the aerodynamic forces from the fluid mesh to the structural one. The first linear mode eigenfrequency is equal to 3.37 Hz which is very close to the frequency of the vortex shedding (3.42Hz). No structural damping was introduced in order to reach high amplitudes of deformation. The partitioned coupling procedure between the fluid solver and the structural nonlinear ROM is summarized in the flowchart Figure 1.

The time integration of the structural solver is performed with the HHT-α method ($\alpha_{HHT} = 0.01$), including Newton-Raphson iterations during each time step. The HHT-α method which belongs to the one-step Newmark's family of time integration methods is more robust to tackle this coupled problem. Indeed, the approximation of the acceleration in the basic Newmark method may induce perturbations that can destabilize the coupling. This problem has been encountered here (as in [55]) and can be avoided with the HHT-α method. The precision of such methods remains of second-order

accuracy but a light numerical damping [56] is introduced, which stabilizes the coupling.

Compared to the previous case without the beam (Fig. 12), the shed vortices strongly interact with the flexible beam and the wake is significantly changed. This interaction produces a complex unsteady aerodynamic forcing that generates beam's vibration with a significant level of amplitude. The maximum level of amplitude is indeed about of the order of magnitude of the cylinder radius. Figure 14 illustrates the coupling during one period in the periodic regime.

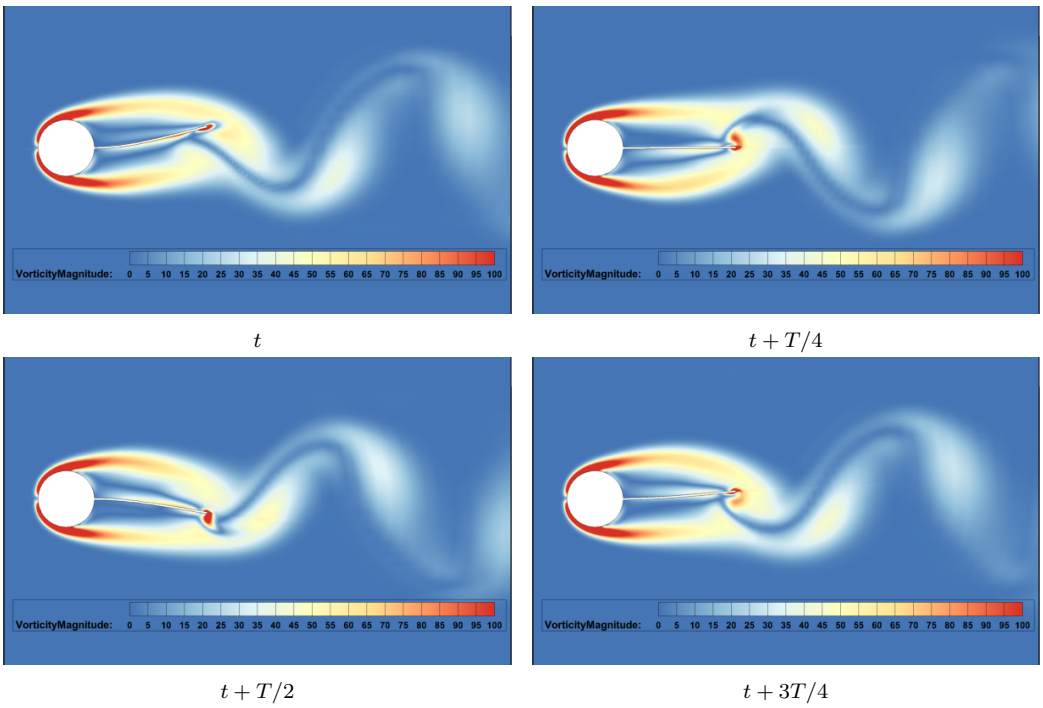

Figure 14: Vorticity magnitude field over one period in the periodic regime of the fluid-structure interaction between the vortices in the wake of the cylinder and the flexible beam.

After a quite long transient, the axial and vertical forces on the beam's wet surface reach a periodic regime whose envelope is visible on Figure 15. Figure 16 illustrates the evolution with time of the vertical and axial displacements at the tip of the beam. The same behavior as for the forces is observed, the displacements converge to a periodic state after a long transient. The maximal vertical displacement reached is about ten times the beam's thickness, i.e. almost the value of the cylinder radius. The maximal axial shortening of the beam is about 1.2 times the beam's thickness: the nonlinearity is therefore significant in this case and has to be properly taken into account in the resolution of the structural dynamics.

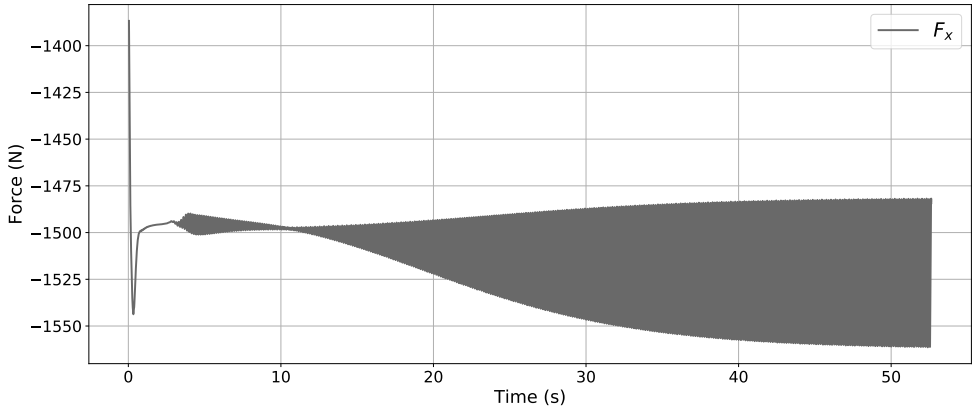

(a) Axial force F_x

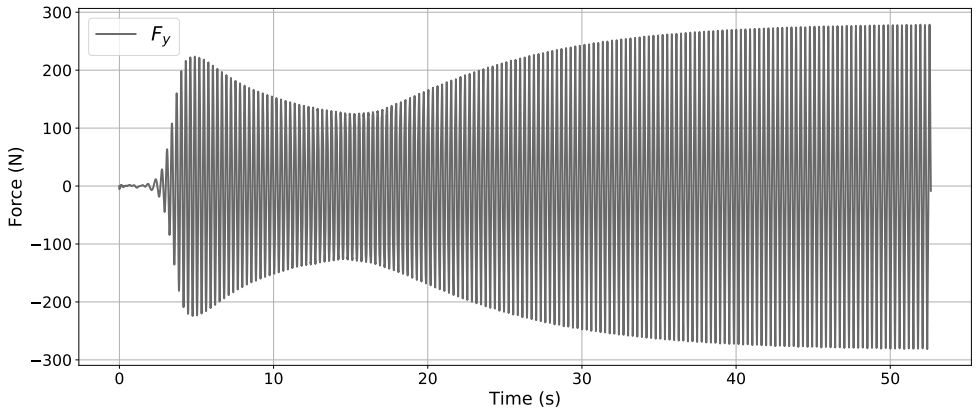

(b) Vertical force F_y

Figure 15: Time evolution of the aerodynamic forces integrated on the surface of the beam. The axial force F_x (a) and vertical force F_y (b).

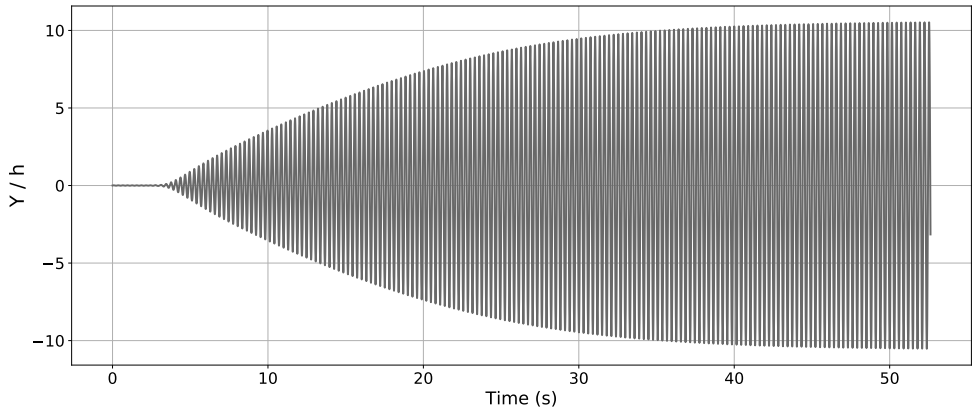

(a) Vertical displacement of the beam tip

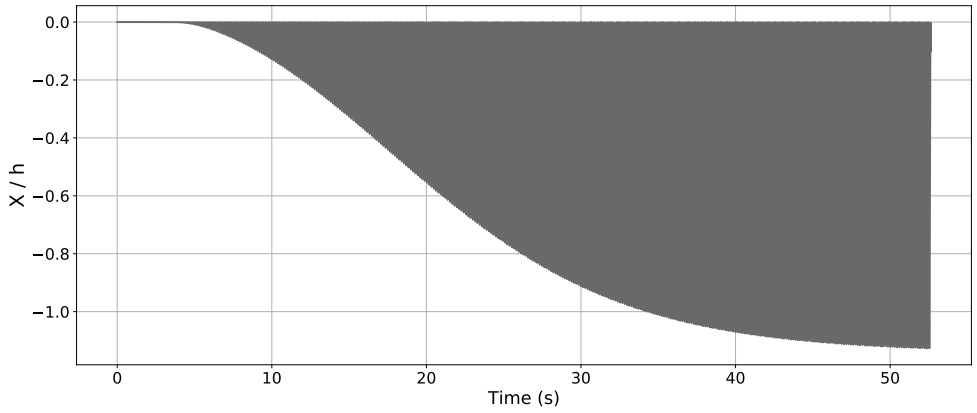

(b) Axial displacement of the beam tip

Figure 16: Evolution of the vertical (a) and axial (b) temporal displacements of the tip of the beam.

To satisfy the fluid-structure equilibrium at a given time step before moving to the next one, fixed-point iterations are carried out between the fluid solver and the structural solver. Figures 17a and 17b represent respectively the evolution of the generalized coordinate of the first mode (resp. the aerodynamic forces projected on the first mode) during the periodic regime. Five fixed-point iterations are performed before moving to the next time step.

The reference solution obtained with the FOM and presented in Figure 16 is now compared in Figure 18 to the linear solution, and to the solution evaluated with the ICDual model for the structure. The ICDual model is the one investigated in section 5, and includes the first three linear normal modes

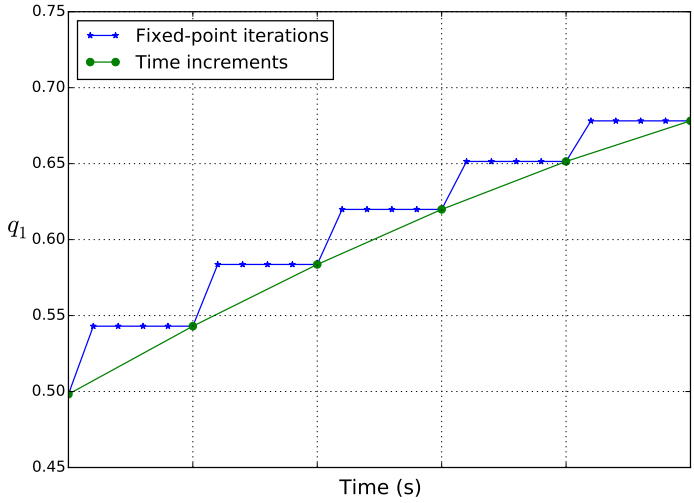

(a) Convergence of the generalized coordinate

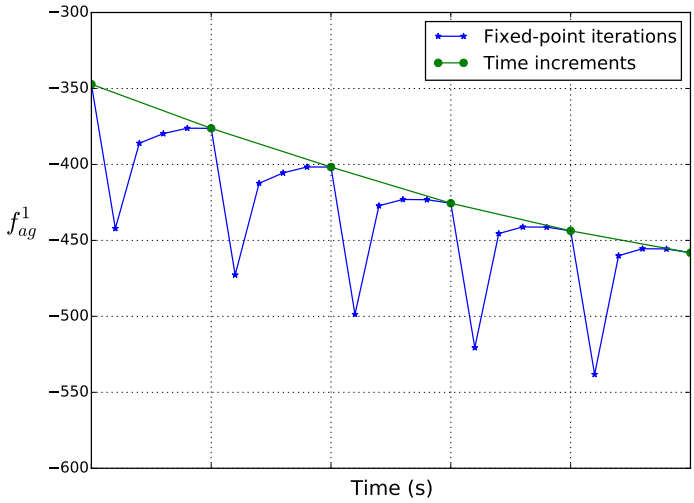

(b) Convergence of the generalized force

Figure 17: Convergence of the generalized coordinate (a) and the aerodynamic force (b) associated to the first mode, during the fixed-point equilibrium loop.

and the five dual modes determined previously to enrich the projection basis. As already reported in section 5 with the purely structural test cases, the linear solution introduces a spurious phase shift and the axial shortening is

not captured at all. For the time interval shown on Figure 18a, the linear response is in advance of two periods with respect to the nonlinear solution: this is illustrated by the horizontal arrow joining the peak values of the linear solution and the corresponding nonlinear solution. The reduced-order model captures precisely (though not exactly) both the vertical and axial displacements during the transient and the periodic regimes.

Finally, the coupled behavior of the beam is investigated over a range of Reynolds number around Re = 200. Indeed, when both the vortex shedding frequency F_s (corresponding to a given Re with Roshko's relation) and the first eigenmode frequency f_0 of the beam are close, a lock-in phenomenon arises and both frequencies match : $F_s = f_0$ for a certain range of Reynolds number. However, when the Reynold number is sufficiently changed, the vortex shedding frequency deviates progressively from the first eigenmode frequency of the beam and the frequencies are no longer locked.

Figures 19 and 20 represent respectively the frequency of vibration of the beam and its vertical amplitude of vibration at the tip as a function of the Reynolds number, evaluated from the coupled aeroelastic solutions computed with linear or non-linear beam formulations. When the frequency of the vortex shedding is far from the eigenmode frequency f_0, the amplitudes of vibration are so small that their frequency is imposed by the fluid flow. However, when the frequency of the vortex shedding is close to f_0, the vibration of the structure and the vortex shedding both respond at a unique frequency for a range of Reynolds numbers. Besides, the range of Reynolds numbers of the plateau slightly differs between the linear and nonlinear cases. The aeroelastic phenomena of lock-in is accurately captured by the ROM solution.

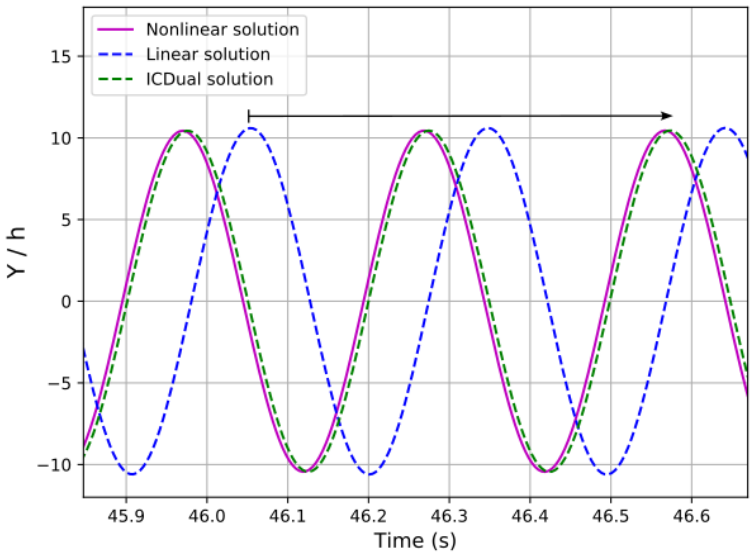

(a) Vertical displacement

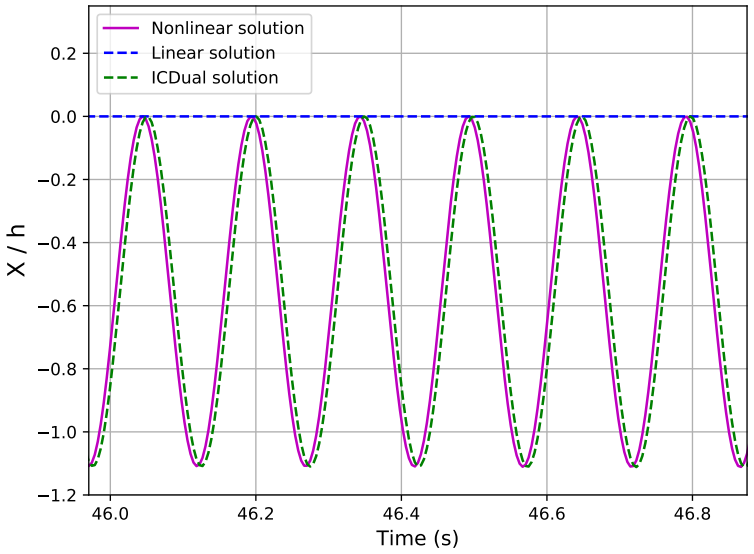

(b) Horizontal displacement

Figure 18: Vertical (a) and axial (b) displacements of the tip of the beam during the aeroelastic coupling in the periodic regime. Comparison between the linear and nonlinear FE solutions and the one obtained with the ICDual ROM.

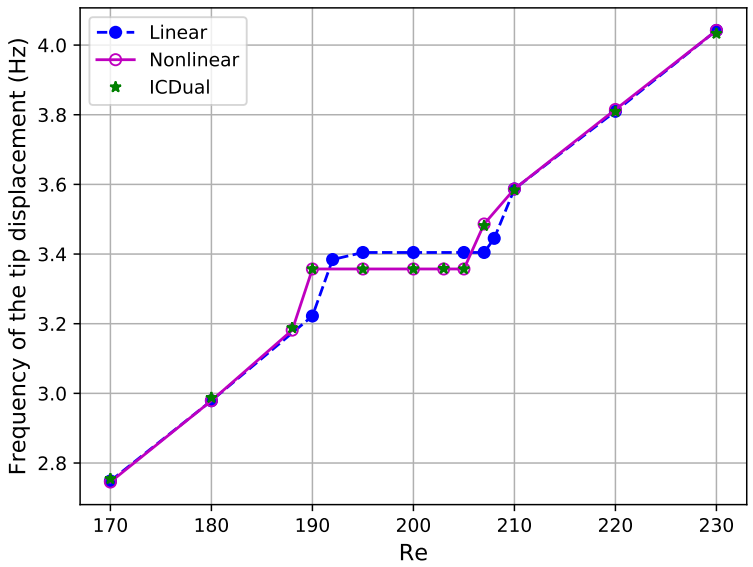

Figure 19: Evolution of the frequency of response of the beam with the Reynolds number of the fluid.

Below and after the range of frequencies characterized by the lock-in phenomenon, the beam responds both at the frequency imposed by the fluid flow and to a lesser extent at the eigenmode frequency f_0. It leads to a beating interference pattern visible in Figures 21a and representing the evolution of the beam tip vertical displacement at Reynolds numbers 180 and 220 respectively. The Fast Fourier Transforms (FFT) of the previous displacements are also illustrated in Figures 21a and 21c, where both frequencies are distinctly noticeable. On the contrary, in the lock-in region, the unsteady response locks on a single frequency, as shown in Figures 21b.

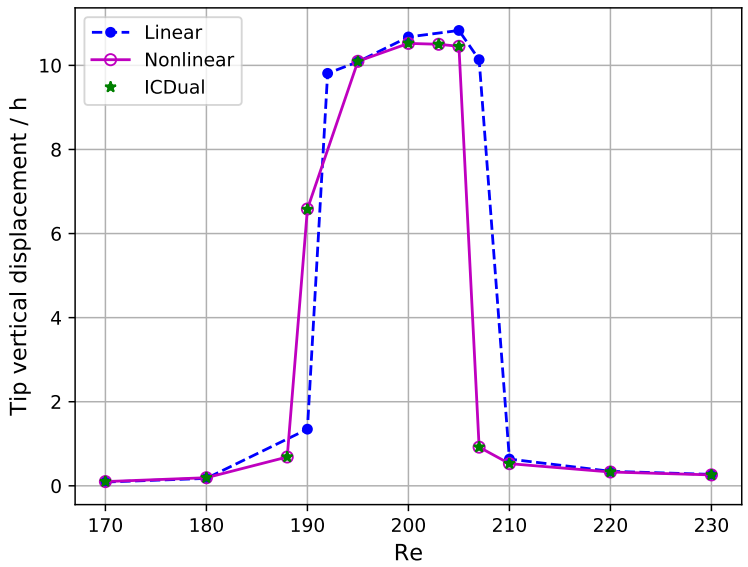

Figure 20: Evolution of the amplitude of vertical displacement at the tip of the beam with the Reynolds number of the fluid.

This last test case demonstrates the potential of coupling a structural ROM based on an original formulation with dual modes for aeroelastic problems. The ICDual ROM matches very accurately the FOM solutions and is easily coupled in the framework of a partitioned approach since the reduced order model is independent from any FE solver. The influence of the structural nonlinearity has finally been highlighted in terms of lock-in frequency and the ROM is able to capture this effect very precisely.

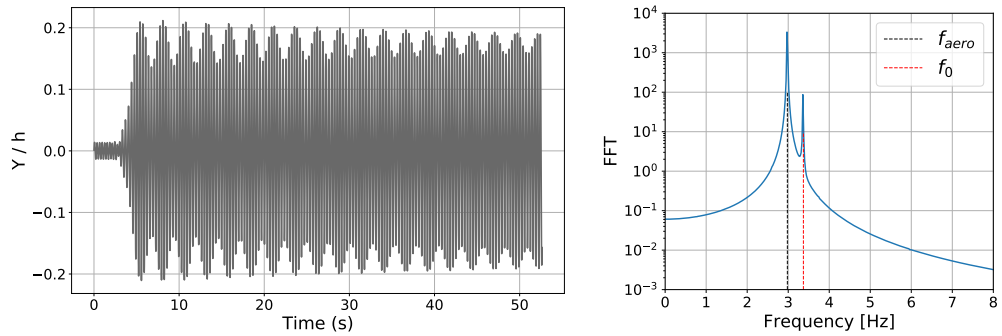

(a) Beam tip vertical displacement in the fluid flow at Reynolds numbers 180: time response (left) and FFT (right)

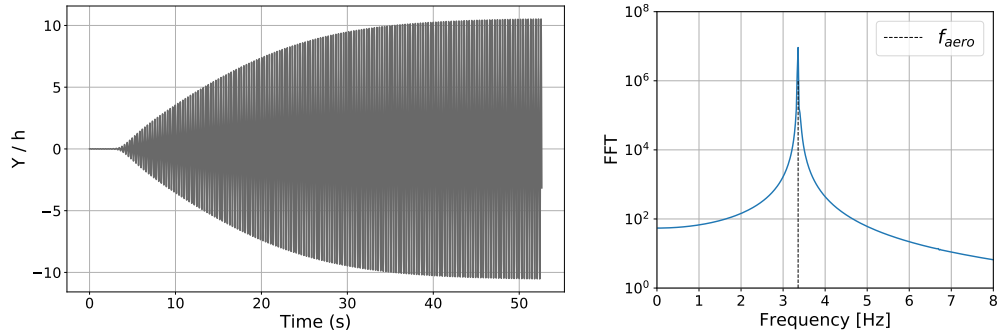

(b) Beam tip vertical displacement in the fluid flow at Reynolds numbers 200: time response (left) and FFT (right)

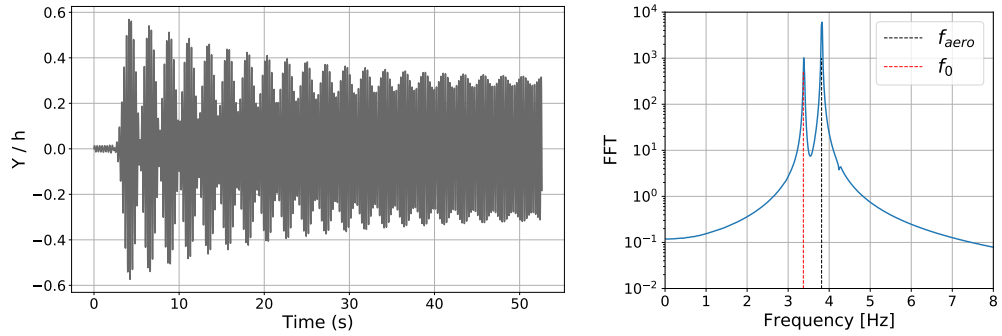

(c) Beam tip vertical displacement in the fluid flow at Reynolds numbers 220: time response (left) and FFT (right)

Figure 21: Temporal evolution and Fast Fourier Transforms of the beam tip vertical displacements in the fluid flow at Reynolds numbers 180, 200 and 220.

7. Conclusion

To compute fluid-structure interaction problems with a partitioned approach, two solvers are used: one for the fluid and one for the solid. The purpose of this paper is to propose a reduced order model only for the structure, while accounting for geometrical nonlinearities. When structures are subject to geometric nonlinearities, the nonlinear interaction between vibration modes of the structure is challenging for projection-based reduced-order models. The choice of the modes in the reduction basis is not trivial compared to linear cases. In this study, dual modes were introduced in the reduction basis, in addition to linear normal modes, in order to capture the geometric nonlinearity of the structure. Besides, this particular ROM has been coupled in the framework of a partitioned approach to a fluid solver. Since the resulting structural ROM is independent from the FE solver, the coupling with the flow solver is made easier. To satisfy this non-intrusiveness condition, an explicit expression of the projected nonlinear forces has to be determined. The projected nonlinear forces were determined explicitly as a polynomial function of the generalized coordinates and the polynomial coefficients were identified by imposing load cases to the structure following the *Implicit Condensation* method. Applied to a Euler-Bernoulli/von Kármán beam, both under local and distributed loads, as well as during a fluid-structure coupling, such a ROM captured very precisely the static and the dynamic responses of the structure. Future work will deal with application of such coupling procedures for more complex three-dimensional flexible structures coupled with high-speed flows. In such 3D cases, the computational time of the structural part predominates when simplified fluid theories (Theodorsen, Lifting-line or Doublet Lattice Method) are used. Even though a high-fidelity fluid formulation is considered in this paper, reduced order models for CFD computations also exist in the literature such as POD, data-driven or hybrid methods. The long term objective is to couple two distinct reduced order models: the one presented in this paper for the structure and another one for the fluid.

8. Acknowledgments

This work was co-financed by the research and innovation program of the European Union Horizon 2020 in the frame of the project Clean Sky 2 ADEC and the platform LPA-IADP.

Appendix A Finite element discretization of the beam

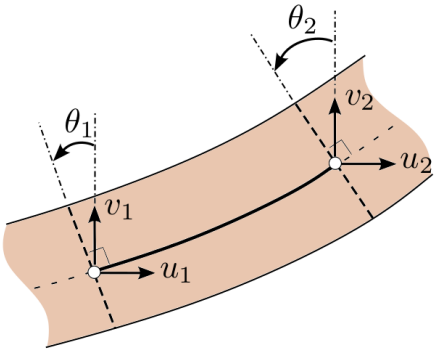

Figure 22: Degrees of freedom in one element of the beam

This appendix provides details on the FE formulation of the Euler-Bernoulli beam with von Kármán hypothesis. Considering one element, the associated nodal values written $u_1, v_1, \theta_1, u_2, v_2, \theta_2$ are represented in Figure 22.

Let $x \in [0, L_e]$ with L_e the length of the element e; the horizontal and vertical displacement in the element write:

$$u_e(x) = N_1(x)u_1 + N_2(x)u_2 \tag{A.1}$$
$$v_e(x) = H_1(x)v_1 + H_2(x)\theta_1 + H_3(x)v_2 + H_4(x)\theta_2, \tag{A.2}$$

or under matrix form for the vector of unknowns $\mathbf{u} = \begin{bmatrix} u_1 & v_1 & \theta_1 & u_2 & v_2 & \theta_2 \end{bmatrix}^T$:

$$\begin{bmatrix} u_e(x) \\ v_e(x) \end{bmatrix} = \mathbf{N}\mathbf{u} \quad \text{with} \quad \mathbf{N} = \begin{pmatrix} \mathbf{N}_\mathrm{u} \\ \mathbf{N}_\mathrm{v} \end{pmatrix} = \begin{pmatrix} N_1 & 0 & 0 & N_2 & 0 & 0 \\ 0 & H_1 & H_2 & 0 & H_3 & H_4 \end{pmatrix}. \tag{A.3}$$

The shape functions $N_1 = 1 - x/L_e$ and $N_2 = x/L_e$ are linear while the shape functions $H_1 = (1 + 2x/L_e)(1 - x/L_e)^2$, $H_2 = x(1 - x/L_e)^2$, $H_3 = x^2(3 - 2x/L_e)/L_e$ and $H_4 = x^2(x/L_e - 1)/L_e$ are 3^{rd} order Hermite functions. Besides, the rotation of the section is given by:

$$\theta_e(x) = \frac{\mathrm{d}v_e(x)}{\mathrm{d}x} = \frac{\mathrm{d}\mathbf{N}_\mathrm{v}(x)}{\mathrm{d}x}\mathbf{u} \equiv \mathbf{N}_\mathrm{v}^{'}\mathbf{u}, \tag{A.4}$$

with

$$\mathbf{N}_{\mathrm{v}}^{'} = \begin{bmatrix} 0 & \dfrac{\mathrm{d}H_1(x)}{\mathrm{d}x} & \dfrac{\mathrm{d}H_2(x)}{\mathrm{d}x} & 0 & \dfrac{\mathrm{d}H_3(x)}{\mathrm{d}x} & \dfrac{\mathrm{d}H_4(x)}{\mathrm{d}x} \end{bmatrix}. \tag{A.5}$$

The mass matrix of one element is computed under the assumption that the local rotational inertia of the section is neglected:

$$\mathbf{M}_e = \frac{\rho A}{2} \int_0^{L_e} \mathbf{N}^T \mathbf{N} \ \mathrm{d}x \tag{A.6}$$

$$= \rho A \frac{L_e}{420} \begin{pmatrix} 140 & 0 & 0 & 70 & 0 & 0 \\ 0 & 156 & 22L_e & 0 & 54 & -13L_e \\ 0 & 22L_e & 4L_e^2 & 0 & 13L_e & -3L_e^2 \\ 70 & 0 & 0 & 140 & 0 & 0 \\ 0 & 54 & 13L_e & 0 & 156 & -22L_e \\ 0 & -13L_e & -3L_e^2 & 0 & -22L_e & 4L_e^2 \end{pmatrix}. \tag{A.7}$$

The linear elastic stiffness matrix of the beam is computed as follows:

$$\mathbf{K}_e = \int_0^{L_e} EA \left(\mathbf{N}_{\mathrm{u}}^{'\,T} \mathbf{N}_{\mathrm{u}}^{'} \right) + EI \left(\mathbf{N}_{\mathrm{v}}^{''T} \mathbf{N}_{\mathrm{v}}^{''} \right) \ \mathrm{d}x \tag{A.8}$$

$$= \frac{EA}{L_e} \begin{pmatrix} 1 & 0 & 0 & -1 & 0 & 0 \\ 0 & 0 & 0 & 0 & 0 & 0 \\ 0 & 0 & 0 & 0 & 0 & 0 \\ -1 & 0 & 0 & 1 & 0 & 0 \\ 0 & 0 & 0 & 0 & 0 & 0 \\ 0 & 0 & 0 & 0 & 0 & 0 \end{pmatrix} + \frac{EI}{L_e^3} \begin{pmatrix} 0 & 0 & 0 & 0 & 0 & 0 \\ 0 & 12 & 6L_e & 0 & -12 & 6L_e \\ 0 & 6L_e & 4L_e^2 & 0 & -6L_e & 2L_e^2 \\ 0 & 0 & 0 & 0 & 0 & 0 \\ 0 & -12 & -6L_e & 0 & 12 & -6L_e \\ 0 & 6L_e & 2L_e^2 & 0 & -6L_e & 4L_e^2 \end{pmatrix}. \tag{A.9}$$

The nonlinear internal forces are computed with a single Gauss point integration to prevent membrane locking, see [49] for the detailed expressions. Their symbolic computation leads to the following expressions:

$$\mathbf{f}_{\mathrm{nl}}^{\mathrm{quad}} = \frac{EA}{32L_e^2} \begin{bmatrix} -\mathbf{f}_{\mathrm{nl}}^{\ a} & -6\mathbf{f}_{\mathrm{nl}}^{\ b} & -L_e\mathbf{f}_{\mathrm{nl}}^{\ b} & \mathbf{f}_{\mathrm{nl}}^{\ a} & 6\mathbf{f}_{\mathrm{nl}}^{\ b} & -L_e\mathbf{f}_{\mathrm{nl}}^{\ b} \end{bmatrix}^T \tag{A.10}$$

$$\mathbf{f}_{\mathrm{nl}}^{\mathrm{cub}} = \frac{EA}{512L_e^3} \begin{bmatrix} 0 & 6\mathbf{f}_{\mathrm{nl}}^{\ c} & L_e\mathbf{f}_{\mathrm{nl}}^{\ c} & 0 & -6\mathbf{f}_{\mathrm{nl}}^{\ c} & L_e\mathbf{f}_{\mathrm{nl}}^{\ c} \end{bmatrix}^T \tag{A.11}$$

with

$$\begin{cases} \mathbf{f}_{\mathrm{nl}}^{\ a} = L_e^2(\theta_1+\theta_2)^2 + 12L_e(\theta_1+\theta_2)(v_1-v_2) + 36(v_1-v_2)^2 \\ \mathbf{f}_{\mathrm{nl}}^{\ b} = 2(u_1-u_2)[L_e(\theta_1+\theta_2) + 6(v_1-v_2)] \\ \mathbf{f}_{\mathrm{nl}}^{\ c} = L_e^2(\theta_1+\theta_2)^2\big[L_e(\theta_1+\theta_2) + 18(v_1-v_2)\big] \\ \qquad\quad + 108(v_1-v_2)^2\big[L_e(\theta_1+\theta_2) + 2(v_1-v_2)\big] \end{cases} \tag{A.12}$$

Appendix B Jacobian of the reduced nonlinear forces

The expression of the projected nonlinear forces in the reduced space is a third-order polynomial of the generalized coordinates. Let $k \in [1, n]$ and $n \geq 3$, the projected non-linear forces in the IC method are:

$$\widetilde{f}_{\mathrm{nl}}^{k}(\mathbf{q}) = \sum_{i=1}^{n}\sum_{j=i}^{n} \beta_{ij}^{k} q_i q_j + \sum_{i=1}^{n}\sum_{j=i}^{n}\sum_{m=j}^{n} \gamma_{ijm}^{k} q_i q_j q_m \tag{B.1}$$

For the resolution of the nonlinear problems, an explicit expression of the jacobian matrix of those internal nonlinear forces is required for the iterative Newton procedure. The coefficient at the line k and the column ℓ of the jacobian matrix of the non-linear forces is equal to:

$$\begin{aligned} \left(\frac{\partial \widetilde{f}_{\mathrm{nl}}^{k}(\mathbf{q})}{\partial q_\ell}\right) &= \frac{\partial}{\partial q_\ell}\left(\sum_{i=1}^{n}\sum_{j=i}^{n} \beta_{ij}^{k} q_i q_j\right) + \frac{\partial}{\partial q_\ell}\left(\sum_{i=1}^{n}\sum_{j=i}^{n}\sum_{m=j}^{n} \gamma_{ijm}^{k} q_i q_j q_m\right) \\ &= \sum_{i=1}^{n} \mathrm{B}_i^{k,\ell} q_i + \sum_{i=1}^{n}\sum_{j=i}^{n} \mathrm{G}_{ij}^{k,\ell} q_i q_j \end{aligned} \tag{B.2}$$

with

$$\mathrm{B}_i^{k,\ell} = \begin{cases} \beta_{i\ell}^{k} & \text{if } i < \ell \\ 2\beta_{\ell\ell}^{k} & \text{if } i = \ell \\ \beta_{\ell i}^{k} & \text{if } i > \ell \end{cases} \tag{B.3}$$

and

$$
\mathrm{G}_{ij}^{k,\ell} = \begin{cases} \text{if } \; j < \ell & \gamma_{ij\ell}^{k} \\ \text{if } \; j = \ell & \begin{cases} 2\gamma_{i\ell\ell}^{k} & \text{if } \; i < \ell \\ 3\gamma_{\ell\ell\ell}^{k} & \text{if } \; i = \ell \end{cases} \\ \text{if } \; j > \ell & \begin{cases} \gamma_{i\ell j}^{k} & \text{if } \; i < \ell \\ 2\gamma_{\ell\ell j}^{k} & \text{if } \; i = \ell \\ \gamma_{\ell i j}^{k} & \text{if } \; i > \ell \end{cases} \end{cases} \tag{B.4}
$$

References

[1] R. Nelson, Simplified calculation of eigenvector derivatives, AIAA Journal 14 (9) (1976) 1201–1205. doi:https://doi.org/10.2514/3.7211.

[2] P. Slaats, J. de Jongh, A. Sauren, Model reduction tools for nonlinear structural dynamics, Computers & Structures 54 (6) (1995-03) 1155–1171. doi:https://doi.org/10.1016/0045-7949(94)00389-K.

[3] J. Rutzmoser, Model order reduction for nonlinear structural dynamics, Ph.D. thesis, Technische Universität München (2018).

[4] M. Karamooz Mahdiabadi, P. Tiso, A. Brandt, D. J. Rixen, A non-intrusive model-order reduction of geometrically nonlinear structural dynamics using modal derivatives, Mechanical Systems and Signal Processing 147 (2021) 107126. doi:https://doi.org/10.1016/j.ymssp.2020.107126.

[5] K. Kim, A. Radu, X. Wang, M. Mignolet, Nonlinear reduced order modeling of isotropic and functionally graded plates, International Journal of Non-Linear Mechanics 49 (2013) 100–110. doi:https://doi.org/10.1016/j.ijnonlinmec.2012.07.008.

[6] M. Mignolet, A. Przekop, S. Rizzi, S. Spottswood, A review of indirect/non-intrusive reduced order modeling of nonlinear geometric structures, Journal of Sound and Vibration 332 (10) (2013) 2437–2460. doi:https://doi.org/10.1016/j.jsv.2012.10.017.

[7] X. Q. Wang, V. Khanna, K. Kim, M. Mignolet, Nonlinear reduced-order modeling of flat cantilevered structures: identification challenges and remedies, Journal of Aerospace Engineering 34 (6) (2021) 04021085. doi:10.1061/(ASCE)AS.1943-5525.0001324.

[8] R. Perez, X. Q. Wang, M. P. Mignolet, Nonintrusive Structural Dynamic Reduced Order Modeling for Large Deformations: Enhancements for Complex Structures, Journal of Computational and Nonlinear Dynamics 9 (3) (02 2014). doi:10.1115/1.4026155.

[9] X. Wang, M. P. Mignolet, Toward a systematic construction of the basis for nonlinear geometric reduced order models, Proceedings of the International Conference on Structural Dynamic , EURODYN 1 (2020) 335 – 354.

[10] C. Touzé, M. Amabili, O. Thomas, Reduced-order models for large-amplitude vibrations of shells including in-plane inertia, Computer Methods in Applied Mechanics and Engineering 197 (21) (2008) 2030–2045. doi:https://doi.org/10.1016/j.cma.2008.01.002.

[11] A. Vizzaccaro, L. Salles, C. Touzé, Comparison of nonlinear mappings for reduced-order modelling of vibrating structures: normal form theory and quadratic manifold method with modal derivatives, Nonlinear Dynamics 103 (4) (2020) 3335–3370. doi:10.1007/s11071-020-05813-1.

[12] A. Vizzaccaro, A. Opreni, L. Salles, A. Frangi, C. Touzé, High Order Direct Parametrisation of Invariant Manifolds for Model Order Reduction of Finite Element Structures: Application to Large Amplitude Vibrations and Uncovering of a Folding Point, Nonlinear Dynamics 110 (1) (2022) 525–571. doi:https://doi.org/10.1007/s11071-022-07651-9.

[13] A. Opreni, A. Vizzaccaro, A. Frangi, C. Touzé, Model order reduction based on direct normal form: application to large finite element MEMS structures featuring internal resonance, Nonlinear Dynamics 105 (2) (2021) 1237–1272. doi:10.1007/s11071-021-06641-7.

[14] G. Haller, S. Ponsioen, Nonlinear normal modes and spectral submanifolds: Existence, uniqueness and use in model reduction, Nonlinear

Dynamics 86 (3) (2016) 1493–1534. doi:https://doi.org/10.1007/s11071-016-2974-z.

[15] S. Jain, P. Tiso, G. Haller, Exact nonlinear model reduction for a von Kármán beam: Slow-fast decomposition and spectral submanifolds, Journal of Sound and Vibration 423 (2018) 195–211. doi:https://doi.org/10.1016/j.jsv.2018.01.049.

[16] C. Touzé, M. Amabili, Nonlinear normal modes for damped geometrically nonlinear systems: Application to reduced-order modelling of harmonically forced structures, Journal of Sound and Vibration 298 (4) (2006) 958–981. doi:https://doi.org/10.1016/j.jsv.2006.06.032.

[17] M. Amabili, C. Touzé, Reduced-order models for nonlinear vibrations of fluid-filled circular cylindrical shells: Comparison of POD and asymptotic nonlinear normal modes methods, Journal of Fluids and Structures 23 (6) (2007) 885–903. doi:https://doi.org/10.1016/j.jfluidstructs.2006.12.004.

[18] M. Li, H. Yan, L. Wang, Nonlinear model reduction for a cantilevered pipe conveying fluid: A system with asymmetric damping and stiffness matrices, Mechanical Systems and Signal Processing 188 (2023) 109993. doi:https://doi.org/10.1016/j.ymssp.2022.109993.

[19] S. Chaturantabut, D. Sorensen, Nonlinear model reduction via discrete empirical interpolation, SIAM Journal on Scientific Computing 32 (5) (2010) 2737–2764. doi:10.1137/090766498.

[20] B. Feeny, R. Kappagantu, On the physical interpretation of proper orthogonal modes in vibrations, Journal of Sound and Vibration 211 (4) (1998) 607–616. doi:https://doi.org/10.1006/jsvi.1997.1386.

[21] G. Kerschen, J. Golinval, Physical interpretation of the proper orthogonal modes using the singular value decomposition, Journal of Sound and Vibration 249 (5) (2001) 849–865. doi:https://doi.org/10.1006/jsvi.2001.3930.

[22] Y. Liang, H. Lee, S. Lim, W. Lin, K. Lee, C. Wu, Proper orthogonal decomposition and its applications, Journal of Sound and Vibration 252 (3) (2002) 527–544. doi:https://doi.org/10.1006/jsvi.2001.4041.

[23] M. Amabili, A. Sarkar, M. Païdoussis, Chaotic vibrations of circular cylindrical shells: Galerkin versus reduced-order models via the proper orthogonal decomposition method, Journal of Sound and Vibration 290 (3) (2006) 736–762. doi:https://doi.org/10.1016/j.jsv.2005.04.034.

[24] M. McEwan, J. Wright, J. Cooper, A. Leung, A combined modal/finite element analysis technique for the dynamic response of a non-linear beam to harmonic excitation, Journal of Sound and Vibration 243 243 (4) (2001) 601–624. doi:https://doi.org/10.1006/jsvi.2000.3434.

[25] J. Hollkamp, R. Gordon, Reduced-order models for nonlinear response prediction: Implicit condensation and expansion, Journal of Sound and Vibration 318 (2008) 1139–1153. doi:https://doi.org/10.1016/j.jsv.2008.04.035.

[26] R. Medeiros, C. E. Cesnik, E. Coetzee, Nonlinear aeroelastic reduced order models using modal coordinates, in: 31st Congress of the International Council of the Aeronautical Sciences, Belo Horizonte, Brazil, 2018.

[27] E. Nicolaidou, T. Hill, S. Neild, Indirect reduced-order modelling: using nonlinear manifolds to conserve kinetic energy, Proceedings of the Royal Society A 476 (2020) 20200589. doi:http://doi.org/10.1098/rspa.2020.0589.

[28] E. Nicolaidou, T. Hill, S. Neild, Nonlinear mapping of non-conservative forces for reduced-order modelling, Proceedings of the Royal Society A (478) (2022) 20220522. doi:https://doi.org/10.1098/rspa.2022.0522.

[29] A. Givois, A. Grolet, O. Thomas, J.-F. Deü, On the frequency response computation of geometrically nonlinear flat structures using reduced-order finite element models, Nonlinear Dynamics 97 (2) (2019) 1747–1781. doi:10.1007/s11071-019-05021-6.

[30] O. Thomas, A. Sénéchal, J.-F. Deü, Hardening/softening behavior and reduced order modeling of nonlinear vibrations of rotating cantilever

beams, Nonlinear Dynamics 86 (2) (2016) 1293–1318. doi:10.1007/s11071-016-2965-0.

[31] S. R. Idelsohn, A. Cardona, A load-dependent basis for reduced nonlinear structural dynamics, Computers & Structures 20 (1) (1985) 203–210, special Issue: Advances and Trends in Structures and Dynamics. doi:https://doi.org/10.1016/0045-7949(85)90069-0.

[32] X. Q. Wang, P. Song, M. P. Mignolet, P. C. Chen, Reduced-order nonlinear damping model: Formulation and application to postflutter aeroelastic behavior, AIAA Journal 59 (10) (2021) 4144–4154. doi:10.2514/1.j059804.

[33] X. Wang, P. Song, M. Mignolet, Applications of multifidelity reduced order modeling to single and multiphysics nonlinear structural problems, Applications in Engineering Science 5 (2021) 100035. doi:10.1016/j.apples.2021.100035.

[34] X. Wang, M. Mignolet, Discussion on "a non-intrusive model-order reduction of geometrically nonlinear structural dynamics using modal derivatives", Mechanical Systems and Signal Processing 159 (2021) 107638. doi:https://doi.org/10.1016/j.ymssp.2021.107638.

[35] A. Muravyov, S. Rizzi, Determination of nonlinear stiffness with application to random vibration of geometrically nonlinear structures, Computers & Structures 81 (15) (2003) 1513–1523. doi:https://doi.org/10.1016/S0045-7949(03)00145-7.

[36] M. P. Mignolet, C. Soize, Stochastic reduced order models for uncertain geometrically nonlinear dynamical systems, Computer Methods in Applied Mechanics and Engineering 197 (45) (2008) 3951–3963. doi:https://doi.org/10.1016/j.cma.2008.03.032.

[37] A. Vizzaccaro, A. Givois, P. Longobardi, Y. Shen, J.-F. Deü, L. Salles, C. Touzé, O. Thomas, Non-intrusive reduced order modelling for the dynamics of geometrically nonlinear flat structures using three-dimensional finite elements, Computational Mechanics 66 (6) (2020-12) 1293–1319. doi:https://doi.org/10.1007/s00466-020-01902-5.

[38] M. Balmaseda, G. Jacquet-Richardet, A. Placzek, D.-M. Tran, Reduced order models for nonlinear dynamic analysis with application to a fan

blade, Journal of Engineering for Gas Turbine and Power 142 (4) (2020) 041002. doi:https://doi.org/10.1115/1.4044805.

[39] D. Liu, P.-C. Chen, Z. Zhang, Z. Wang, S. Yang, D.-H. Lee, M. Mignolet, F. Liu, N. Lindsley, P. Beran, Continuous dynamic simulation for morphing wing aeroelasticity, 2009. doi:10.2514/6.2009-2572.

[40] R. Perez, X. Wang, M. P. Mignolet, Prediction of displacement and stress fields of a notched panel with geometric nonlinearity by reduced order modeling, Journal of Sound and Vibration 333 (24) (2014) 6572–6589. doi:https://doi.org/10.1016/j.jsv.2014.06.014.

[41] A. Matney, R. Perez, P. Song, X. Wang, M. P. Mignolet, S. M. Spottswood, Thermal-structural reduced order models for unsteady/dynamic response of heated structures in large deformations, Applications in Engineering Science 12 (2022) 100119. doi:https://doi.org/10.1016/j.apples.2022.100119.

[42] J. J. Hollkamp, R. W. Gordon, S. M. Spottswood, Nonlinear modal models for sonic fatigue response prediction: a comparison of methods, Journal of Sound and Vibration 284 (3) (2005) 1145–1163. doi:https://doi.org/10.1016/j.jsv.2004.08.036.

[43] A. Frangi, G. Gobat, Reduced order modelling of the non-linear stiffness in MEMS resonators, International Journal of Non-Linear Mechanics 116 (2019) 211–218. doi:https://doi.org/10.1016/j.ijnonlinmec.2019.07.002.

[44] R. Tibshirani, Regression Shrinkage and Selection via the Lasso., Journal of the Royal Statistical Society Series B: Statistical Methodology 58 (1) (1996) 267–288.

[45] H. Zou, T. Hastie, Regularization and Variable Selection Via the Elastic Net, Journal of the Royal Statistical Society Series B: Statistical Methodology 67 (5) (2005) 768–768. doi:10.1111/j.1467-9868.2005.00527.x.

[46] J. Donea, A. Huerta, J.-P. Ponthot, A. Rodríguez-Ferran, Arbitrary Lagrangian–Eulerian Methods 1 (2004) 413–437. doi:https://doi.org/10.1002/0470091355.ecm009.

[47] L. Cambier, S. Heib, S. Plot, The Onera elsA CFD software: input from research and feedback from industry, Mechanics Industry 14 (3) (2013) 159–174. doi:10.1051/meca/2013056.

[48] A. Dugeai, A. Madec, A.-S. Sens, Numerical unsteady aerodynamics for turbomachinery aeroelasticity, in: 9th International Symposium of Unsteady Aerodynamics, Aeroacoustics and Aeroelasticity of Turbomachines, Lyon (France), 2000.

[49] J. N. Reddy, An Introduction to nonlinear Finite Element Analysis Ed. 2, Oxford university press, NY, 2015.

[50] S. Turek, J. Hron, Proposal for numerical benchmarking of fluid–structure interaction between an elastic object and laminar incompressible flow, in: Fluid–Structure Interaction: Modelling, Simulation, Optimisation, Springer-Verlag, H.J. Bungartz, M. Schäfer (Eds.), Berlin, Heidelberg, Netherlands, 2006, pp. 371–385.

[51] M.-S. Liou, C. J. Steffen, A new flux splitting scheme, Journal of Computational Physics 107 (1) (1993) 23–39. doi:https://doi.org/10.1006/jcph.1993.1122.

[52] I. Mary, P. Sagaut, M. Deville, An algorithm for unsteady viscous flows at all speeds, International Journal for Numerical Methods in Fluids 34 (5) (2000) 371–401. doi:https://doi.org/10.1002/1097-0363(20001115)34:5<371::AID-FLD54>3.0.CO;2-W.

[53] A. Roshko, On the development of turbulent wakes from vortex streets, Ph.D. thesis, California Institute of Technology (1952).

[54] F.-B. Tian, H. Dai, H. Luo, J. F. Doyle, B. Rousseau, Fluid-structure interaction involving large deformations: 3d simulations and applications to biological systems, Journal of Computational Physics 258 (2014) 451–469. doi:10.1016/j.jcp.2013.10.047.

[55] G. De Nayer, Interaction Fluide-Structure pour les corps élancés, Ph.D. thesis, Ecole Centrale de Nantes (ECN) (Dec. 2008).

[56] D. J. Rixen, M. Géradin, Mechanical Vibrations, Theory and Application to Structural Dynamics Ed. 3, John Wiley & Sons, UK, 2015.